

1-1-2007

Charge transfer between nitrogen cations and nitrogen at low energies

Wayn K Ward
University of Nevada, Las Vegas

Follow this and additional works at: <https://digitalscholarship.unlv.edu/rtds>

Repository Citation

Ward, Wayn K, "Charge transfer between nitrogen cations and nitrogen at low energies" (2007). *UNLV Retrospective Theses & Dissertations*. 2274.
<http://dx.doi.org/10.25669/lmof-eau2>

This Thesis is protected by copyright and/or related rights. It has been brought to you by Digital Scholarship@UNLV with permission from the rights-holder(s). You are free to use this Thesis in any way that is permitted by the copyright and related rights legislation that applies to your use. For other uses you need to obtain permission from the rights-holder(s) directly, unless additional rights are indicated by a Creative Commons license in the record and/or on the work itself.

This Thesis has been accepted for inclusion in UNLV Retrospective Theses & Dissertations by an authorized administrator of Digital Scholarship@UNLV. For more information, please contact digitalscholarship@unlv.edu.

CHARGE TRANSFER BETWEEN N^{2+} AND N_2 AT LOW ENERGIES

by

Wayn K Ward

Bachelor of Science
Mesa State College
2004

A thesis submitted in partial fulfillment
of the requirements for the

**Master of Science Degree in Physics
Department of Physics and Astronomy
College of Sciences**

**Graduate College
University of Nevada, Las Vegas
December 2007**

UMI Number: 1452286

INFORMATION TO USERS

The quality of this reproduction is dependent upon the quality of the copy submitted. Broken or indistinct print, colored or poor quality illustrations and photographs, print bleed-through, substandard margins, and improper alignment can adversely affect reproduction.

In the unlikely event that the author did not send a complete manuscript and there are missing pages, these will be noted. Also, if unauthorized copyright material had to be removed, a note will indicate the deletion.

UMI[®]

UMI Microform 1452286

Copyright 2008 by ProQuest LLC.

All rights reserved. This microform edition is protected against unauthorized copying under Title 17, United States Code.

ProQuest LLC
789 E. Eisenhower Parkway
PO Box 1346
Ann Arbor, MI 48106-1346



Thesis Approval

The Graduate College
University of Nevada, Las Vegas

November 9th, 2007

The Thesis prepared by

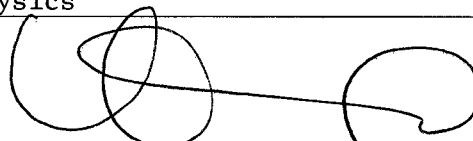
Wayn Kauimakaokalani Ward

Entitled

Charge Transfer Between N^{2+} and N_2 at Low Energies

is approved in partial fulfillment of the requirements for the degree of

Masters of Science in Physics



Examination Committee Chair

Dean of the Graduate College

Examination Committee Member

Examination Committee Member

Graduate College Faculty Representative

Examination Committee Member

ABSTRACT

Charge Transfer Between N^{2+} and N_2 at Low Energies

by

Wayn K. Ward

Dr. Victor H. S. Kwong, Examination Committee Chair

Professor of Physics

University of Nevada, Las Vegas

The measurement of charge transfer rate coefficients between multiply charged ions and neutral atoms and molecules is important in the areas of plasma physics and astrophysics. Such a measurement is also essential in verifying various theoretical electron capture processes. N^{2+} is of particular interest since it is abundant in astrophysical nebulae and interstellar molecular clouds. The charge transfer rate coefficient for the charge exchange reaction between N^{2+} [$2s^22p\ (^2P^0)$] and N_2 is measured using ion trap techniques. N^{2+} ions are produced by electron impact ionization of N_2 and stored inside a cylindrical rf trap. The charge transfer rate coefficient is determined by measuring the decay rate of stored N^{2+} ions in the ion trap. The measured charge transfer rate coefficient between N^{2+} and N_2 is $1.95 \pm 0.27 \times 10^{-9} \text{ cm}^3 \text{ s}^{-1}$ at $T_{equiv} = 9.1 \times 10^3 \text{ K}$. The estimated uncertainty of $\pm 14\%$ is mainly due to the statistical fluctuations of the ion signal and the N_2 particle density measurements. The charge transfer rate coefficient is within one standard deviation of previously published results.

TABLE OF CONTENTS

ABSTRACT	iii
LIST OF FIGURES	v
ACKNOWLEDGMENTS	v
CHAPTER 1 INTRODUCTION	1
CHAPTER 2 THEORETICAL BACKGROUND	4
The Classical Approach	5
CHAPTER 3 EXPERIMENTAL FACILITIES	10
The Vacuum System	10
Cylindrical RF Quadrupole Ion Trap	14
Electron Gun	22
Ion Detection System	22
Gas Delivery System	24
Experimental Timing Electronics	26
Data Acquisition/Analysis System	28
CHAPTER 4 EXPERIMENTAL METHODS AND PROCEDURES	32
Experimental Method and General Procedure	32
Creation of N^{2+}	33
Ion Selection and Storage	35
Ion Detection	39
Pressure Calibration	40
Data Analysis	41
CHAPTER 5 DISCUSSION OF RESULTS AND CONCLUSIONS	44
REFERENCES	56
VITA	59

LIST OF FIGURES

Figure 1	Potential Curve Crossing	6
Figure 2	Classical Orbiting Model of a Charge Transfer Process	7
Figure 3	Experimental Facilities	11
Figure 4	The Vacuum Chamber	12
Figure 5	The Vacuum System	13
Figure 6	Stability Diagram of the Ion Trap	19
Figure 7	Geometry of the Cylindrical RF Quadrupole Ion Trap	20
Figure 8	Configuration of the Ion Trap	21
Figure 9	a) TOF Spectrum of N^{2+} b) Stability Diagram for N^{2+}	25
Figure 10	Experimental Timing and Control Signals	27
Figure 11	a) RF Terminated on Falling Edge b) Field Lines Within Ion Trap	29
Figure 12	a) RF Terminated on Rising Edge b) Field Lines Within Ion Trap	30
Figure 13	Data Acquisition and Analysis System	31
Figure 14	Least-Squares Fit of a Typical Time Dependent N^{2+} Signal	34
Figure 15	Residual Background Gas	36
Figure 16	a) Stability Diagram for N^+ and N^{2+} b) Time of Flight for N^+ and N^{2+} ...	37
Figure 17	a) Stability Diagram for N^+ and N^{2+} b) Time of Flight for N^{2+}	38
Figure 18	Decay Curves of N^{2+}	45
Figure 19	Charge Transfer Rate Coefficient Between N^{2+} and N_2	47
Figure 20	N^{2+} Decay Curve	50
Figure 21	N^{2+} Decay Curve	51
Figure 22	N^{2+} Decay Curve	52
Figure 23	N^{2+} Decay Curve	53
Figure 24	N^{2+} Decay Curve	54
Figure 25	N^{2+} Decay Curve	55

ACKNOWLEDGMENTS

I wish to acknowledge the numerous people who made this thesis possible. First and foremost, I would like to thank my advisor, Dr. Victor H. S. Kwong and my committee members Dr. James Selser, Dr. David Shelton, Dr. Stephen Lepp, and Dr. Balakrishnan Naduvalath for their helpful guidance and suggestions along the way.

I am also grateful to Bill O'Donnell, Chrysanthos Kyriakides, Brad Clarke, Matthew Jacobsen, Daniel Antonio, and Tae Song Lee for all of their collaboration and encouragement.

Finally, I wish to thank my parents for all the emotional support and assistance that they have provided on the journey leading up to this point. I would not be the person that I am today without them.

CHAPTER 1

INTRODUCTION

A charge transfer reaction occurs when charge is passed between one atomic or molecular system and another. In some reactions this charge may involve a single electron, while in others it may involve multiple electrons. Charge transfer reactions between multiply charged ions and neutral molecules at eV energies have proven to be one of the most difficult basic collision processes to predict reliably. This is due to the complicated electronic, rotational, and vibrational configurations of the particles in question and the accuracy of the potential surfaces of the quasi-molecule formed [1].

Noteworthy applications of charge transfer reactions between multiply charged ions and neutral molecules at low energies include:

1. Astrophysics:

In the interstellar cloud, multiply charged ions are formed and coexist with neutral atoms and molecules. Electron capture during collisions plays a crucial role in the charge state balance and the characterization of cosmic plasmas and astronomical objects [2]. Charge transfer processes involving carbon ions, for example, are of particular interest since carbon ions are abundant in astrophysical objects [2].

2. Thermonuclear fusion research:

Investigating certain charge transfer rates will help develop an understanding of the interactions between hydrogen and impurity ions at the edge and core of tokamak fusion plasmas. A large amount of the impurity ions are generated when hot plasma ions strike the limiter and the wall of the tokamak. Therefore, the edge plasma has the highest concentration of impurities and charge transfer between those ions and

neutrals can occur rapidly [3]. The properties of the edge plasma have a significant impact on plasma energy confinement as well [3]. This is due to the fact that the edge plasma dictates the boundary conditions for the system and the impurities in the edge plasma may travel to the center plasma and radiate away energy in the process [4].

3. Short wavelength lasers:

Charge transfer may provide a possible pumping mechanism for population inversion in short wavelength lasers. Therefore, understanding certain charge transfer processes would prove valuable in the creation of x-ray or vacuum ultraviolet laser light [5].

4. Verifying theoretical calculations:

Measurement of charge transfer processes is important for verifying theoretical models of the electron capture process. The quantal calculation of charge transfer processes at low energies is far from exact. Although the theory's accuracy has increased in recent years, many discrepancies still exist not only between individual calculations, but also between the experimentally measured values and the calculated ones. The experimentally measured charge transfer rate coefficient between O^{2+} and He [6], for example, disagrees with the quantal calculations [7] by up to three orders of magnitude. The quantal calculations, however, vary by up to five orders of magnitude themselves [7], [8]. Therefore, actually measuring charge transfer rate coefficients helps to refine existing theoretical calculations.

There are quite a few methods used to study charge transfer collisions between multiply charged ions and neutrals. The ion trap methodology was used for the results presented in this thesis since it is known to accommodate energies well below 1 eV/amu [9]. The ion source in this approach utilizes electron impact dissociative ionization of a molecular gas, or electron impact ionization of an atomic gas [10], [11].

The focus of this work is on the measurement of the charge transfer rate coefficient between N^{2+} and N_2 at low energies. Since N^{2+} is only 44 eV above its neutral ground

state, it can easily be produced by the electron impact ionization technique of the ion trap approach. N^{2+} is of particular interest, as it is present in significant amounts in astrophysical nebulae, nova shells, and interstellar molecular clouds [12], [13]. These ions may also play an important role in the production of N^+ [1]. Furthermore, molecular nitrogen might contribute to impurities found at the edge of fusion reactors [1].

This thesis will be presented in the following manner. Chapter 2 addresses the physics behind charge transfer. Chapter 3 describes the experimental facilities that were used to take the measurements. Chapter 4 covers the experimental methods and procedures utilized to carry out the measurements. Finally, in Chapter 5, the experimental results are presented and a discussion on the possible sources of error and how the results compare with previous measurements are given.

CHAPTER 2

THEORETICAL BACKGROUND

The discovery of charge transfer is credited to G.H. Henderson in 1923. As he passed alpha particles through absorbing screens of mica, he observed numerous He^+ ions and neutral He atoms exiting the far side of his experimental setup [14]. Henderson surmised that the He atoms and ions were being created because the alpha particles were capturing electrons from within the mica screens. This belief was later confirmed in 1924 by Rutherford [15].

In 1927, Thomas used classical mechanics to generate the first theoretical model explaining charge transfer [16]. The following year Oppenheimer [17] and Brinkman and Kramers [18] developed a theoretical model that used quantum mechanics and perturbation techniques. Utilizing quantum mechanics to explain charge transfer is rather difficult since it involves finding the stationary states of the nuclei and electrons involved in the reaction process and it is impossible to solve the Schrodinger equation exactly for such a system. There are, however, approximation techniques available to solve this problem [15]. Those methods will not be covered in this thesis since they are beyond the scope of this work.

Since low energies (less than 1 eV/amu) were used in this experiment, a quasi-molecular model of charge transfer was used to describe the interactions that take place between the N^{2+} and N_2 particles [3]. A quasi-molecule is formed when the nuclei of two colliding atoms/molecules or ions approach each other so closely that the electron to be captured is simultaneously shared by the two nuclei [19]. The idea of a quasi-molecule was first proposed in 1933 by Massey and Smith [20].

The charge transfer process that takes place in this experiment is of the form



where A^{q+} is a multiply charged ion and B is a neutral molecule. A quasi-molecule is formed

when A^{q+} approaches B . This approach is symbolized by an attractive potential curve as seen in Fig.(1). When the multiply charged ion and neutral begin to separate, there is a finite probability that an electron will be transferred from the multiply charged ion to the neutral molecule. If this happens, the particles will then follow the repulsive Coulomb potential curve designated as $A^{(q-1)+} + B^+$ in Fig.(1) [3]. If the charge transfer reaction is exothermic, or releases energy, then the curves described in Fig.(1) will cross and charge transfer is likely to occur [21].

The Classical Approach

When an ion with charge q approaches an atom/molecule, the collision dynamics between the two particles become dominated by the ion induced polarization of the target atom/molecule [22]. At low energies this leads to an attractive polarization force between the atom/molecule and the ion and the trajectory of the incoming ion deviates from its original path [Fig.(2)]. This is the basis of the Langevin model. According to this simple classical model, the interaction potential ($V(R)$) is defined in cgs units as

$$V(R) = -\frac{\alpha q^2}{2R^4}, \quad (2.2)$$

where R is the internuclear distance between the ion and atom/molecule and α is the polarizability of the target atom/molecule [3]. The polarizability is the tendency of a charge distribution, such as the electron cloud of an atom or molecule, to become distorted from its normal shape by the electric field of a nearby ion or dipole [15].

The total energy (E_0) of the ion-atom/molecule pair is defined to be

$$E_0 = T(R) + V(R). \quad (2.3)$$

Here $T(R)$ is the kinetic energy of the atom/molecule ion pair as a function of the internuclear separation between them. Combining Eq.(2.2) and Eq.(2.3),

$$E_0 = T(R) - \frac{\alpha q^2}{2R^4}. \quad (2.4)$$

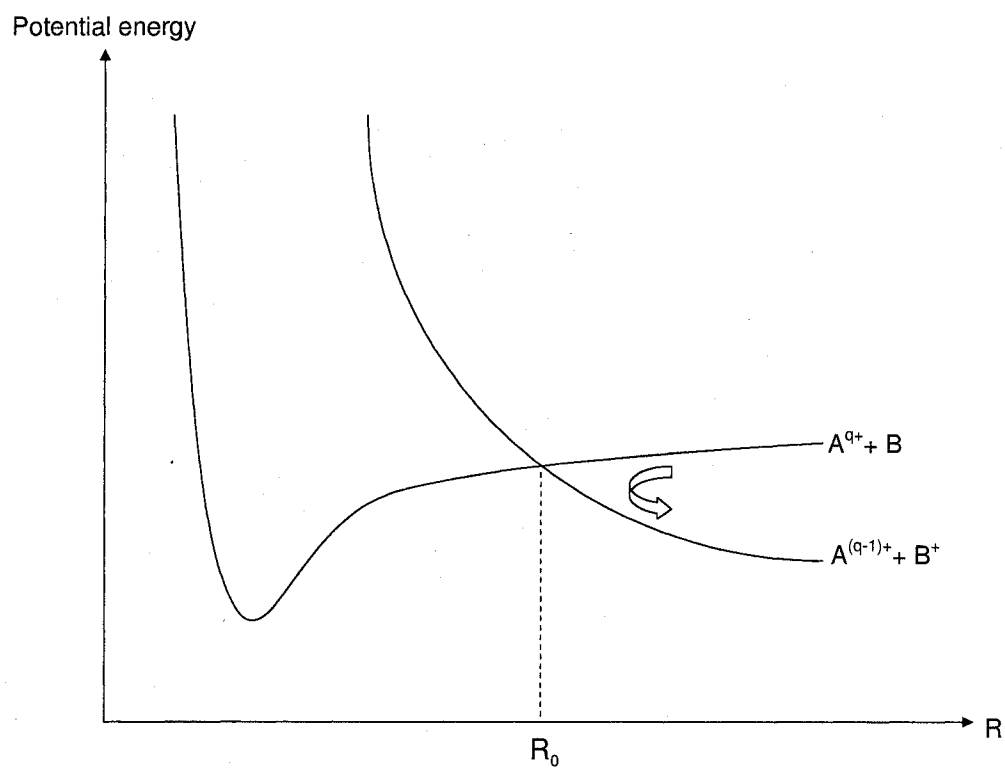


Figure 1 Potential Curve Crossing

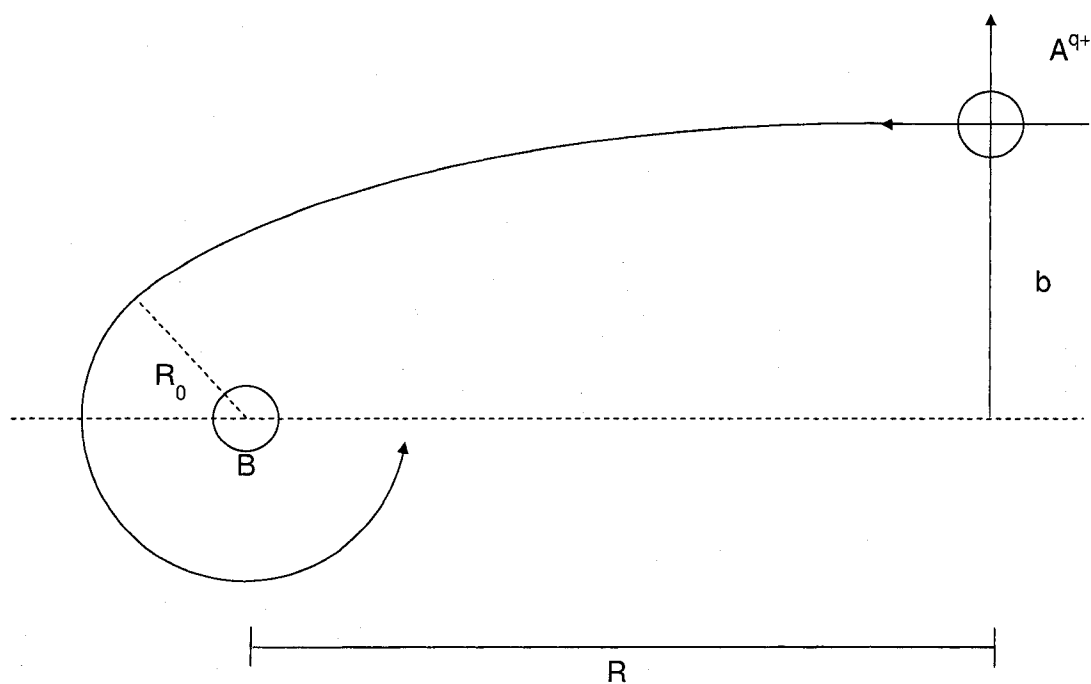


Figure 2 Classical Orbiting Model of a Charge Transfer Process

When the atom/molecule and the ion reach the point of closest approach, $R = R_0$ and the ion will orbit the atom/molecule only if the attractive dipole force (F_D) balances the centripetal force (F_C) [3]. When that happens, the atom/molecule and ion will remain close to one another long enough for electron exchange to take place. In other words,

$$F_D = -\nabla V(R) = \frac{2\alpha q^2}{R_0^5} = F_C = \frac{\mu v^2}{R_0} \quad (2.5)$$

and

$$T(R_0) = \frac{1}{2}\mu v^2, \quad (2.6)$$

where μ is the reduced mass of the atom/molecule and ion system. Therefore,

$$\frac{2\alpha q^2}{R_0^5} = \frac{2T(R_0)}{R_0}. \quad (2.7)$$

Solving Eq.(2.7) for $T(R_0)$,

$$T(R_0) = \frac{\alpha q^2}{R_0^4}, \quad (2.8)$$

and inserting the result into Eq.(2.4),

$$E_0 = \frac{\alpha q^2}{2R_0^4}. \quad (2.9)$$

Upon rearranging Eq.(2.9), the radius of closest approach can be defined in terms of the ionization state (q) of the ion, the polarizability (α) of the target atom/molecule, and the total energy (E_0) of the atom/molecule ion pair:

$$R_0 = \left[\frac{\alpha q^2}{2E_0} \right]^{\frac{1}{4}}. \quad (2.10)$$

Next, the scattering cross section can be calculated by employing the conservation of angular momentum since in general,

$$\mathbf{L} = \mathbf{r} \times \mathbf{p} = rp \sin \Theta = rp. \quad (2.11)$$

and

$$E = \frac{p^2}{2m} \quad (2.12)$$

Therefore, combining Eq.(2.11) and Eq.(2.12) yields

$$L^2 = E2mr^2. \quad (2.13)$$

Upon using Eq.(2.13) and comparing the initial angular momentum of the atom/molecule and ion system to its final angular momentum,

$$T(R_0)R_0^2 = E_0b^2. \quad (2.14)$$

Thus, the impact parameter (b) is of the form

$$b = \left[\frac{2\alpha q^2}{E_0} \right]^{\frac{1}{4}}. \quad (2.15)$$

The cross section (σ) is defined to be

$$\sigma = \pi b^2. \quad (2.16)$$

Substituting Eq.(2.15) into Eq.(2.16),

$$\sigma = \pi \left[\frac{2\alpha q^2}{E_0} \right]^{\frac{1}{2}}. \quad (2.17)$$

According to Eq.(2.17), the charge transfer cross section is dependent on the ionization state (q) of the ion, the polarizability (α) of the atom/molecule, and the total energy (E_0) of the atom/molecule and ion system. E_0 is calculated from the estimated relative velocity between the ion and atom/molecule pair. For the charge transfer reaction between N^{2+} and N_2 , the upper bound of the cross section is estimated to be $4.04 \times 10^{-15} \text{ cm}^2$.

CHAPTER 3

EXPERIMENTAL FACILITIES

The experimental facilities used to measure the charge transfer rate coefficient between N^{2+} and N_2 at low energies include an ultra-high vacuum system, a cylindrical rf quadrupole ion trap, an ion creation system, an ion detection system, a gas delivery system, a timing control system, and a data acquisition and analysis system. A schematic of the facilities used is shown in Fig.(3).

The Vacuum System

The vacuum system used in this experiment produces a high vacuum environment with a background pressure of 5×10^{-11} Torr. As Fig.(4) shows, the stainless steel (304) vacuum chamber consists of a main compartment that houses the ion trap assembly. This assembly, which is mounted to one of the chamber's six ports, is composed of an ion trap and an electron gun. The vacuum chamber is pumped by a Varian Turbo V-550 turbomolecular pump that is backed by a Varian SD-450 mechanical pump. A foreline trap located on the mechanical pump's intake is used to prevent pump oil from back streaming into the turbomolecular pump [Fig.(5)].

The vacuum system and the turbomolecular pump are protected by an automatic shut-down system. This system is controlled by an electronic switching circuit. It consists of a cooling water flow sensor switch and a pneumatic valve with a thermocouple (TC) vacuum gauge. The cooling water flow sensor monitors the rate at which water is flowing through the turbomolecular pump. In order for the pump to operate at a certain temperature, it needs to dissipate the frictional heat buildup generated by its high rotation speeds. To accomplish that, water has to flow through the pump at a minimum rate. The switch will turn the

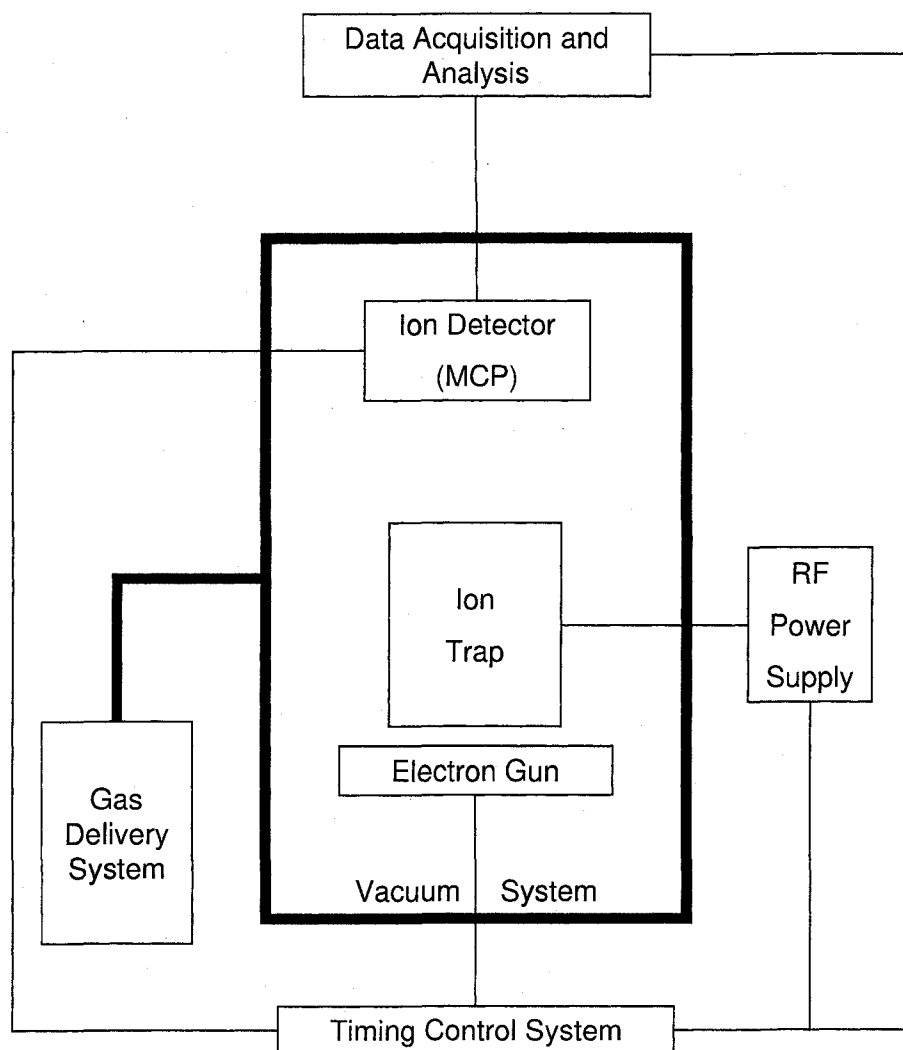


Figure 3 Experimental Facilities

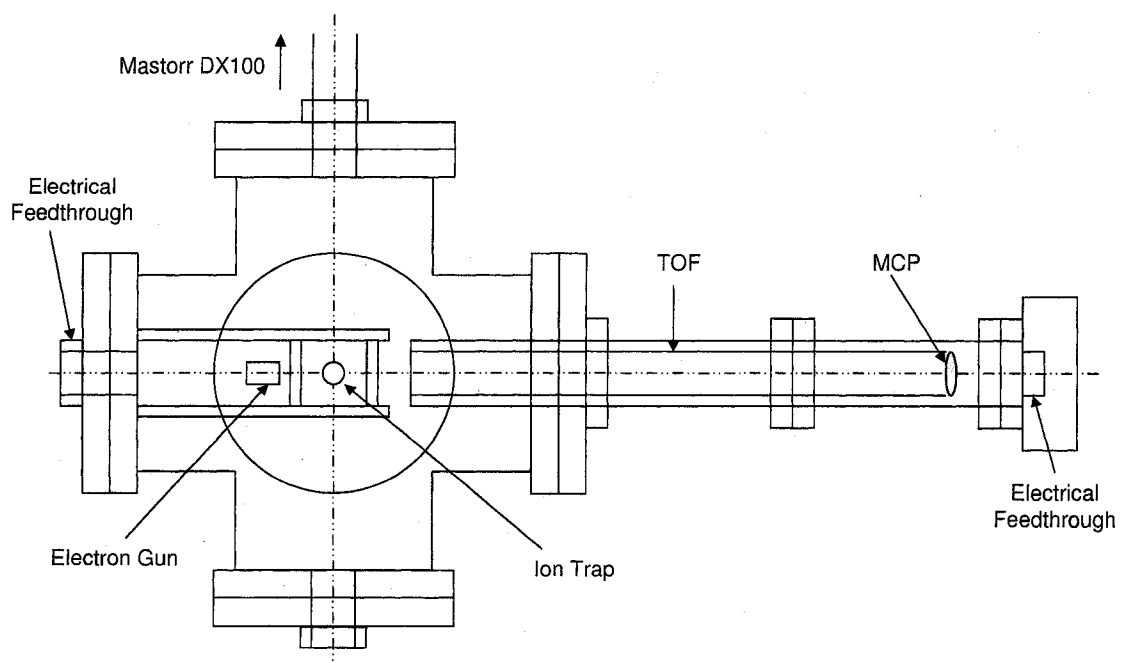


Figure 4 The Vacuum Chamber

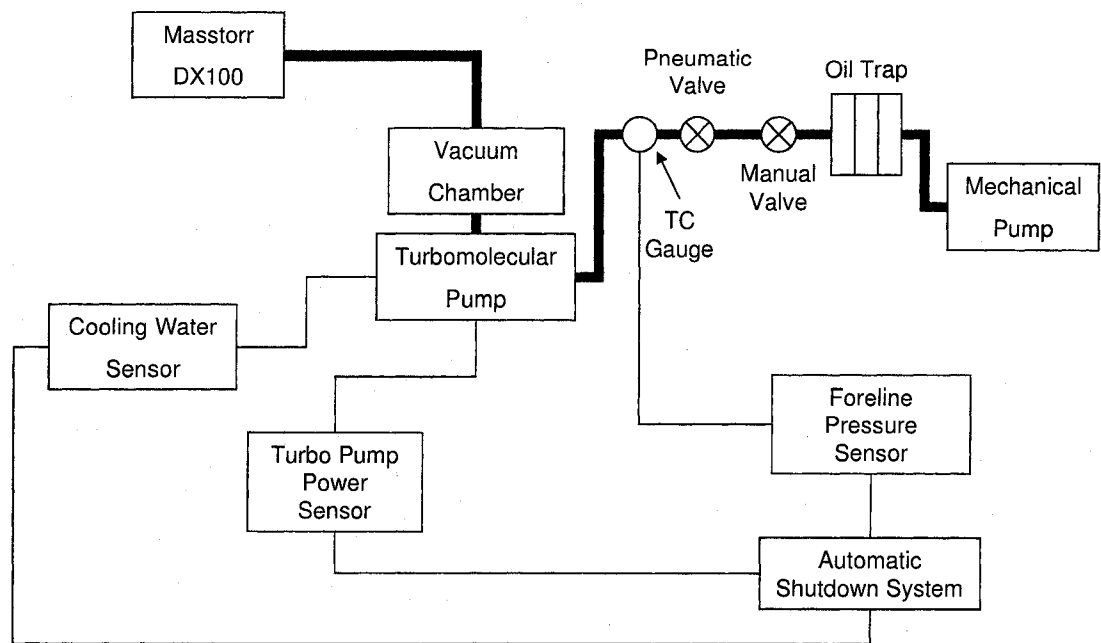


Figure 5 The Vacuum System

turbomolecular pump off and isolate the vacuum chamber if the water flow rate falls below an acceptable level. The pneumatic valve is located between the mechanical pump and the turbomolecular pump. It is driven by high pressure nitrogen gas. If for some reason the foreline pressure measured by the thermocouple gauge exceeds the preset threshold of 100 mTorr, the valve automatically isolates the vacuum chamber and the turbomolecular pump from the mechanical pump. This prevents mechanical pump oil and other contaminants from reaching the vacuum chamber in the event of a foreline vacuum failure.

The configuration of the six port stainless steel ultra-high vacuum chamber used in the experiment is shown in Fig.(4). The bottom port is connected to the turbomolecular pump. Attached to the back port are a residual gas analyzer (Masstorr DX100) and a leak valve used in the gas delivery system. The ion trap assembly and electrical feedthrough are mounted on the left port of the vacuum chamber. The time of flight (TOF) tube and the multichannel plate (MCP) are attached to the right port. The top and front ports are equipped with quartz viewing windows and sealed by 20 cm flanges. The top port also features a leak valve through which helium can be introduced into the system. Helium is used to improve ion peak signal resolution when measurements of the residual background of the vacuum system are taken.

With this vacuum system setup, a residual background pressure of 5×10^{-11} Torr can be obtained without baking. This residual pressure can be attributed to the H_2 , H_2O , and CO molecules that attach themselves to the vacuum chamber walls. The pressure in the vacuum chamber can be measured by the ion gauge (Masstorr DX100) in total mode.

Cylindrical RF Quadrupole Ion Trap

The most important aspect of the facility used in this experiment is its ability to confine specific ions to a particular volume for an extended period of time with minimal perturbation. This feat is achieved by using a cylindrical rf quadrupole ion trap. The trap utilizes a relatively weak (~ 50 V/cm) radio frequency field to create a pseudopotential for storing ions. Further information about this process can be found in Dehmelt's review articles [23]. Detailed discussions on ion traps can also be found in numerous other publications and

papers [23], [24].

The rf quadrupole ion trap is a three dimensional evolution of the quadrupole mass filter developed by Paul [25]. Its feasibility was first demonstrated by Berkling [26] and Fischer [27]. Since then, several studies have been conducted on the properties of the quadrupole ion trap. Most notable among these are Dawson et al. [28] – [40] and Todd et al. [37], [41] – [45]. They carried out extensive investigations on ion traps with hyperbolic electrodes. The first theoretical study of a cylindrical ion trap was performed by Benilar and Audion in 1973 [46].

Unlike an ion trap with hyperbolic electrodes, there is no simple solution for the potential distribution of an ion trap with a cylindrical electrode. Fortunately, it has been shown that the potential surfaces near the center of a cylindrical ion trap approximate those produced by ideal hyperbolic electrodes [46]. Since the ions are stored near the center of the trap in this experiment, the theoretical description of the potential distribution for the hyperbolic ion trap can be used as a guide to describe the potential distribution inside the cylindrical ion trap.

The form of the hyperbolic potential distribution inside the cylindrical ion trap is given by the following equation:

$$\Phi(r, z) = \frac{U(t)}{r_0^2 + 2z_0^2} [r^2 - 2(z^2 - z_0^2)], \quad (3.1)$$

where

$$U(t) = U_0 + V_0 \cos \Omega t \quad (3.2)$$

is the time dependent potential being applied to the ring electrode of the ion trap [47].

When a charged ion is located within such a potential distribution, it will see an electric field of the form

$$\mathbf{E} = -\nabla \Phi(r, z), \quad (3.3)$$

and experience a radial and axial force given by

$$F_r = eE_r = m\ddot{r} \quad (3.4)$$

and

$$F_z = eE_z = m\ddot{z} \quad (3.5)$$

respectively.

As a result, the equations of motion for an ion with a mass m with a charge e located within the ion trap become

$$\ddot{r} + \frac{e}{m} \frac{2U_0}{r_0^2 + 2z_0^2} r + \frac{e}{m} \frac{2V_0}{r_0^2 + 2z_0^2} r \cos \Omega t = 0, \quad (3.6)$$

$$\ddot{z} - \frac{e}{m} \frac{4U_0}{r_0^2 + 2z_0^2} r - \frac{e}{m} \frac{4V_0}{r_0^2 + 2z_0^2} z \cos \Omega t = 0. \quad (3.7)$$

If one defines

$$a_z = -2a_r = \frac{-16eU_0}{m(r_0^2 + 2z_0^2)\Omega^2}, \quad (3.8)$$

$$q_z = -2q_r = \frac{8eV_0}{m(r_0^2 + 2z_0^2)\Omega^2}, \quad (3.9)$$

and sets

$$\nu = \frac{\Omega t}{2}, \quad (3.10)$$

it can be shown through algebraic manipulation that both the r and z equations of motion have the form

$$\frac{d^2 u}{d\nu^2} + (a - 2q \cos 2\nu)u = 0. \quad (3.11)$$

This is the Mathieu equation. Its solutions are known to possess well defined regions that result in bounded stable motion [24]. The two parameters a and q determine an ion's

trajectory within the trap. They are related to an ion's charge state (e) and mass (m), the ion trap's length ($2z_0$) and radius (r_0), and the rf frequency ($f = \frac{\Omega}{2\pi}$), rf amplitude (V_0), and DC bias (U_0) applied to the ring electrode [Eq.(3.8) and Eq.(3.9)]. Figure 6 illustrates the stability diagram obtained when the values of a_z , a_r , q_z , and q_r are such that motion is stable in both the axial and radial directions. Selecting the voltages (V_0 , U_0) and frequency (f) that are applied to the ring electrode determines the location (a_z , q_z) of an ion with a certain charge to mass ratio on this diagram. An ion will be stored only if it lies within the region marked stable.

The potential well depths in the axial and radial direction can also be obtained from the Mathieu equation [24]. They are defined as

$$D_z = \left[\frac{4eV_0^2}{m(r_0^2 + 2z_0^2)^2\Omega^2} - \frac{2U_0}{(r_0^2 + 2z_0^2)} \right] z_0^2, \quad (3.12)$$

$$D_r = \left[\frac{eV_0^2}{m(r_0^2 + 2z_0^2)^2\Omega^2} + \frac{U_0}{(r_0^2 + 2z_0^2)} \right] r_0^2. \quad (3.13)$$

These potential well depths help determine the mean energy of the ions stored within the trap. It has been experimentally shown that the mean energy of ions located within the trap is approximately one tenth of the shallowest potential well depth (D_z or D_r) [48]. Since the velocity distribution of the ions in a rf trap with hyperbolic electrodes is Maxwellian, the velocity of the stored ions can be characterized by a temperature (T_i) [49]. The ion temperature is related to the mean energy of the stored ions through the following equation

$$\overline{E} = \frac{3}{2}kT_i. \quad (3.14)$$

Because the temperature of the neutral reactant gas is at room temperature (300 K), an equivalent temperature of the collisional system corresponding to the mean relative velocity of N^{2+} and the reactant N_2 gas molecules needs to be introduced. This equivalent temperature (T_{equiv}) is given by

$$\frac{T_{equiv}}{\mu} = \frac{T_i}{m_i} + \frac{T_n}{m_n}, \quad (3.15)$$

where the ion temperature is T_i and the reactant gas temperature is T_n [50]. The masses of the ion and the neutral are m_i and m_n respectively, while μ is their reduced mass.

The optimum trapping parameters were investigated both theoretically and experimentally. Mathematica was used to solve the Mathieu equation and produce an interactive stability diagram of the ion trap potential as shown in Fig.(6) [51]. This was used to identify values of the rf amplitude (V_0), DC bias (U_0), and rf frequency (f) needed to trap ions of a particular mass to charge ratio. These values (V_0 , U_0 , and f) were then tested on the actual cylindrical trap.

The physical configuration of the cylindrical rf quadrupole ion trap used in this experiment is shown in Fig.(7) and Fig.(8). The trap is comprised of a cylindrical ring electrode and two flat end caps. The ring electrode has a radius of 1.67 cm and a length of 3.34 cm. Both the ring electrode and the end caps are constructed from 30 gauge 304 stainless steel mesh. Stainless steel mesh was used because of its ability to maintain a rigid structure and its inherent high conduction. Four symmetric holes (each 5 mm in diameter) are cut into the ring electrode. This was done to allow laser beams clear passage through the trap. No lasers were used in this measurement.

The cylindrical geometry was chosen for three main reasons:

1. It was easy to machine and assemble compared to a hyperbolic trap.
2. It was felt that the four symmetric holes that had to be cut in the ring electrode would perturb the electric fields within a cylindrical trap to a smaller degree than a hyperbolic trap [52].
3. It provided a straightforward and non-invasive means of ion extraction when compared to a hyperbolic trap.

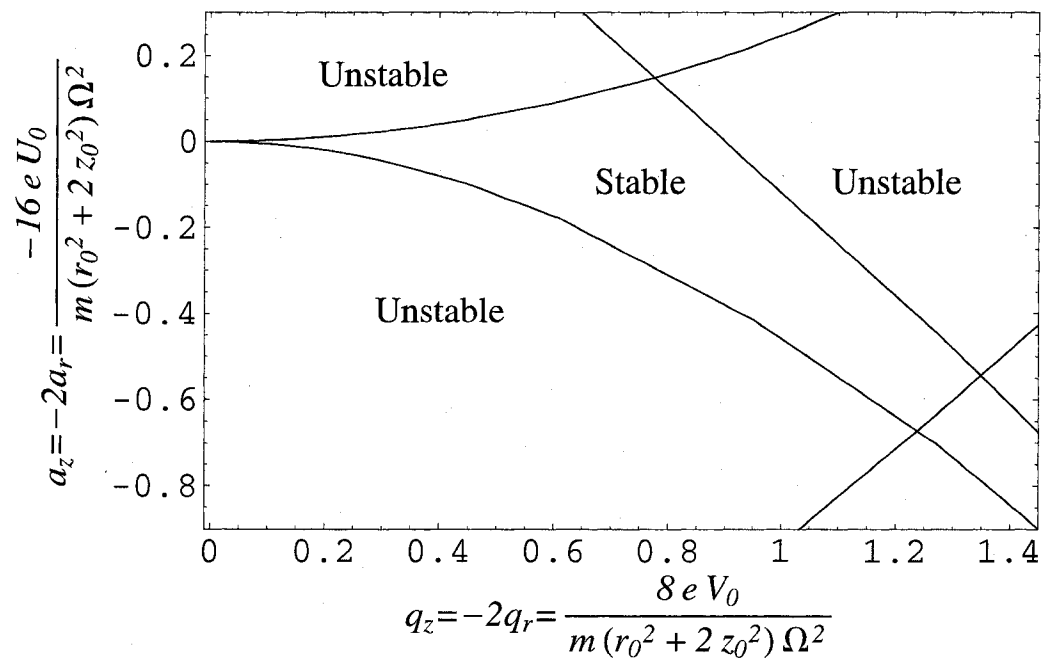


Figure 6 Stability Diagram of the Ion Trap

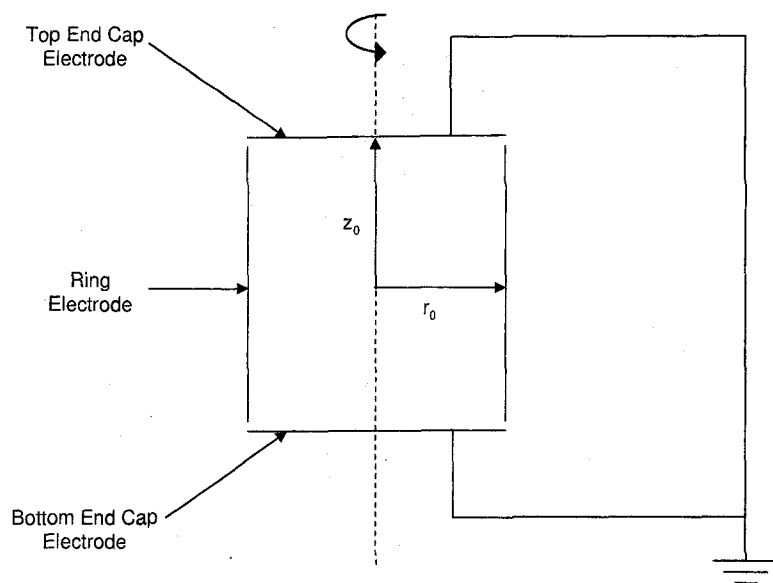


Figure 7 Geometry of the Cylindrical RF Quadrupole Ion Trap

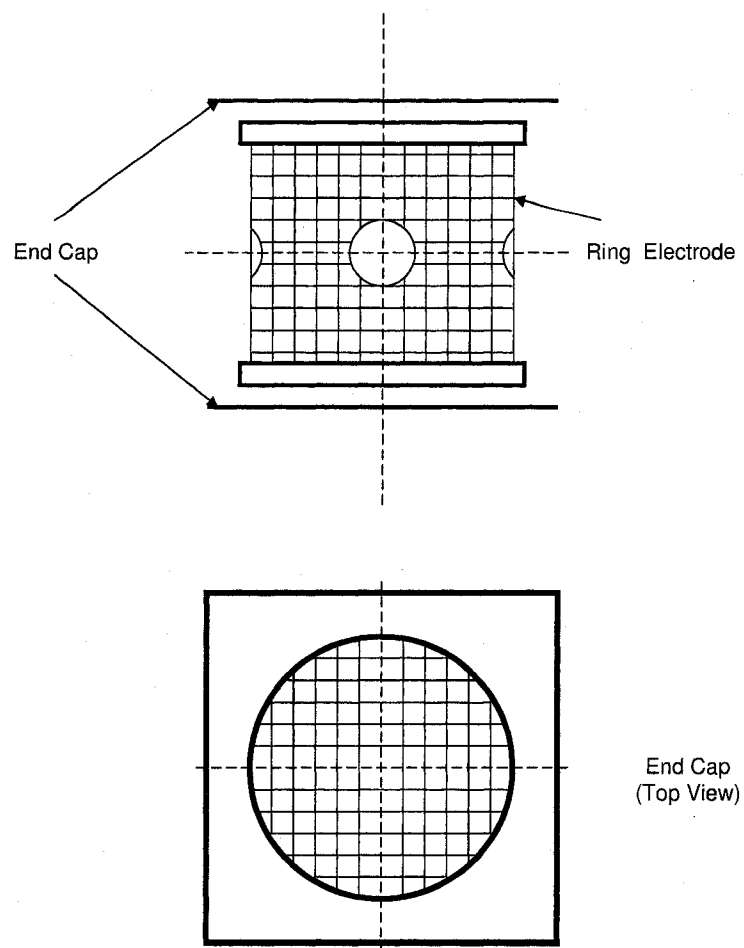


Figure 8 Configuration of the Ion Trap

Electron Gun

The Spectra-Mat BaO-based electron gun is the main component of the ion creation system used for this experiment. It produces electrons which in turn generate ions by means of electron impact ionization of atomic and molecular gases. The electron gun is attached to a ceramic standoff and mounted in close vicinity to the ion trap [Fig.(4)]. The electron gun filament is comprised of tungsten and barium oxide. This combination of materials was chosen because it allows higher emission current densities at lower operating temperatures [53]. During the experiment, the cathode was heated by passing a current of ~ 1.0 A through it and applying a potential difference of +4.8 V across it.

In order to generate the N^{2+} ions needed for the experiment, the electron gun was given a bias voltage of -150 V while the end caps of the ion trap were grounded. With these parameters, the electrons produced by the electron gun were accelerated into the ion trap and created N^{2+} . In addition, the electrons can be confined to the region around the electron gun when necessary by providing the electron gun with a bias of $+210$ V. This prevents unwanted electrons from reaching the ion trap and disturbing the charge transfer rate coefficient measurement.

Ion Detection System

A pair of high gain Burle 25 mm microchannel plates (MCPs) is used to sample ions that were stored in the cylindrical rf ion trap. The plates, which operate in vacuum, are oriented in a chevron configuration and mounted at the end of the time of flight (TOF) tube [Fig.(4)].

Each MCP is made up of an array of miniature channel electron multipliers that have been fused together in the form of a thin disc. These multipliers, which are oriented parallel to one another in a honeycomb configuration, are 5 microns in diameter and consist of a hollow glass tube with an internal resistive surface processed for high secondary emission. In order to promote secondary emission, the MCP has a large potential difference ($+1850$ V) applied across it. When a positively charged ion encounters the low potential end of the plate it enters a channel and collides with the channel wall. This collision produces several

secondary electrons. These secondary electrons are accelerated down the channel by the potential difference across the MCP and produce even more electrons by colliding with the channel walls along the way. This process is repeated numerous times along the channel, and a large number of electrons (a minimum of 10^7 at +2400 V) finally leave the high potential output.

From there, the signal is sent through an amplifier and ultimately displayed as a time of flight spectrum on a Tektronix TDS 680C oscilloscope. The spectrum is digitized by the oscilloscope and sent directly to a Gateway E-4200 computer for storage and analysis. All the data used in the final analysis of the charge transfer rate coefficient between N^{2+} and N_2 was obtained with a MCP detector.

For this experiment, two methods of ion identification are used. They are the time of flight method and the stability region method. The time of flight method simply uses the experimentally verified mass to charge ratio and time of flight value associated with a known ion to determine the mass to charge ratio or time of flight value of another ion. Since all the ions removed from the rf trap see the same extraction potential, the time of flight of an ion observed on the oscilloscope (t_2) can be related to its mass to charge ratio ($\frac{m_2}{q_2}$) by the following equation

$$\frac{m_2}{q_2} = \frac{m_1}{q_1} \left(\frac{t_2}{t_1} \right)^2, \quad (3.16)$$

where $\frac{m_1}{q_1}$ and t_1 are the mass to charge ratio and the time of flight of a known ion respectively. Using this relation, one can determine the mass to charge ratio of an ion signal displayed on the oscilloscope simply by using its time of flight value.

Solving Eq.(3.16) for t_2 , one gets

$$t_2 = \left[\frac{m_2}{q_2} \frac{q_1}{m_1} \right]^{1/2} t_1. \quad (3.17)$$

With this relation, one can solve for the value of t_2 at which the ion signal should be displayed

on the oscilloscope. This method is used for this experiment. Since the mass to charge ratio of N^{2+} is already known ($\frac{m}{q} = 7$) it is just a matter of locating the ion signal corresponding to the correct time of flight value for N^{2+} . In order to do that, C^+ , with a known mass to charge ratio of 12 and time of flight value of $4.65 \mu s$ is used. Using Eq.(3.17) then, it can be shown that N^{2+} should have a time of flight of around $3.60 \mu s$. Figure 9a shows the TOF spectrum of N^{2+} .

The second technique used to identify ions is the stability diagram method. As previously discussed, the stability diagram is generated by using Mathematica to solve the Mathieu equation. Adjusting the DC bias (U_0) and the rf amplitude (V_0) inputs shift the position of ions in the stability diagram. Higher mass to charge ratio ions can be excluded from the trap by adjusting the trapping parameters (f , V_0 , U_0) until the ions fall below the edge of the stable region. As seen in Fig.(9a), the experimentally obtained time of flight spectrum is consistent with the rf ion trap settings and behavior suggested by the stability diagram in Fig.(9b).

Gas Delivery System

During the period of time that the charge transfer rate coefficient measurement was carried out, the vacuum system was filled with ultrahigh purity molecular nitrogen gas. The N_2 gas pressure ranged from 3.60×10^{-8} to 2.44×10^{-7} Torr. This was much larger than the normal vacuum system background pressure of 5×10^{-11} Torr.

The copper gas lines and gas reservoir were first pumped down to less than 30 mTorr by a mechanical pump equipped with a cold trap. This was done to remove impurities that may have been left over from previous measurements. The reservoir was then filled with molecular nitrogen gas. From there, the N_2 gas was introduced into the system through a leak valve located on the back port of the vacuum chamber. The level of purity of the N_2 gas was then checked by using the ion gauge (Masstorr DX100).

The rate at which the N_2 gas was introduced into the system through the leak valve over the course of the measurement was comparable to the rate at which the turbomolecular pump removed the N_2 gas from the system. This ensured that the N_2 gas pressure stayed

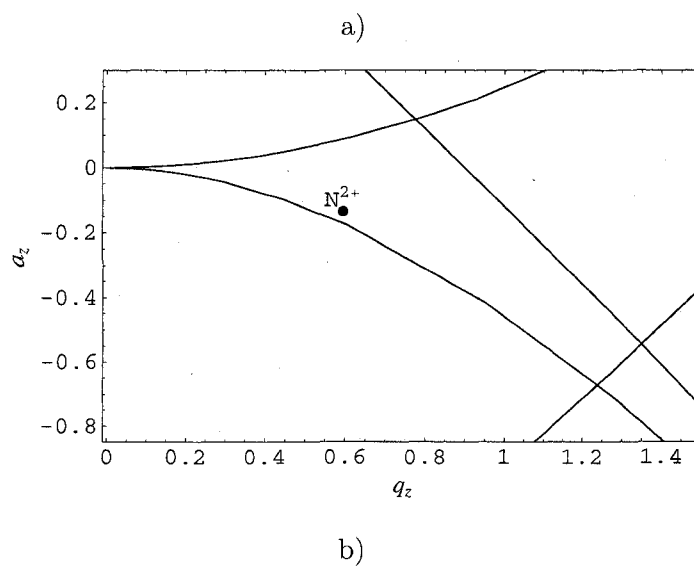
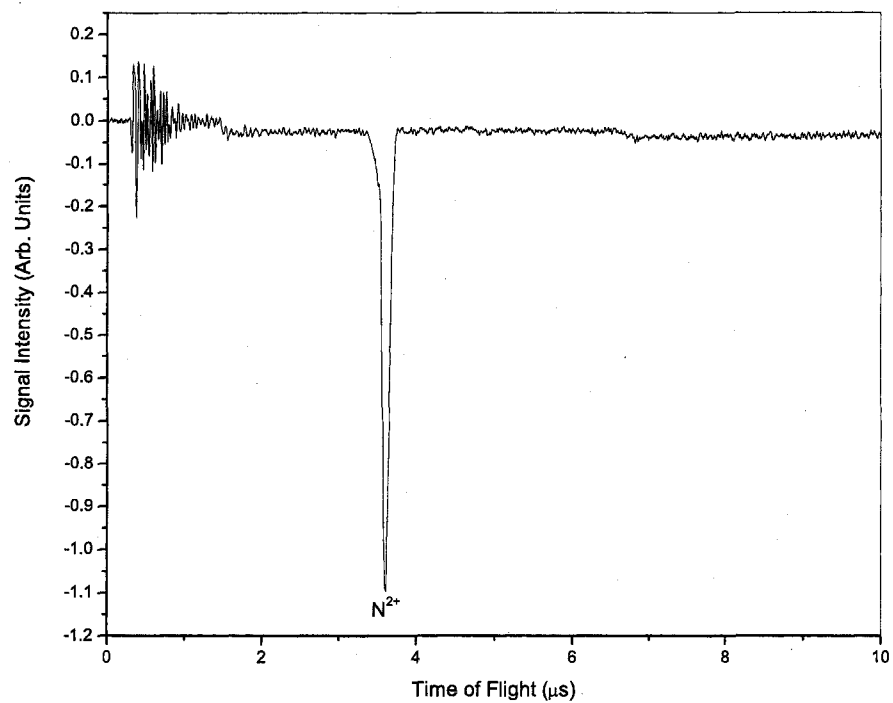


Figure 9 a) TOF Spectrum of N^{2+} b) Stability Diagram for N^{2+}

relatively constant. The Masstorr DX100 was used to determine the pressure of the N_2 gas in the vacuum chamber before and after each measurement. It was turned off for the duration of each measurement. This was due to the fact that the ion gauge was observed to produce ions that were captured by the ion trap.

Experimental Timing Electronics

The driving force behind the experimental timing electronics is the Ion Storage Pulse Interval Controller (IS-PIC). It contains logic circuitry that generates four transistor to transistor logic (TTL) timing pulses. A diagram of these pulses is outlined in Fig.(10).

Starting from $t = 0$, the first pulse created by the IS-PIC controls the ionization period. The length of this pulse determines how long the electron gun will be allowed to pulse electrons into the trap. The falling edge of this first pulse triggers the relaxation pulse. The duration of this second pulse is defined as the period of time from when the electron gun is shut off to the generation of the detection pulse. The detection pulse, which is the third pulse created by the IS-PIC, is turned on by the falling edge of the relaxation pulse. The rising edge of the detection pulse also turns on the MCP. The fourth pulse, triggered by the falling edge of the detection pulse, initiates the extraction of the ions from the trap. This extraction is caused by temporarily terminating the rf waveform (f , V_0 , U_0) being applied to the ring electrode of the ion trap and placing a positive (+236 V) and negative (−225 V) potential on opposite end caps of the trap in order to push/pull the ions from the trap.

The rising edge of the fourth pulse, or dump pulse, is synchronized to a specific phase of the rf waveform. It has been experimentally shown that the location at which the rf waveform is terminated plays a crucial role in the stored ion clouds shape and size [54].

When the rf potential is terminated as the falling edge of the sinusoidal waveform crosses the zero point [Fig.(11a)], the resulting ion time of flight signal that is observed on the oscilloscope has broad peaks with poor resolution. This is due to the direction that the rf field lines are pointing within the trap as the ion cloud is ejected. As Fig.(11b) illustrates, the field lines progress from the ring electrode to the grounded endcaps. Therefore, as the positively charged ion cloud is ejected from the ion trap, it is compressed in the x direction

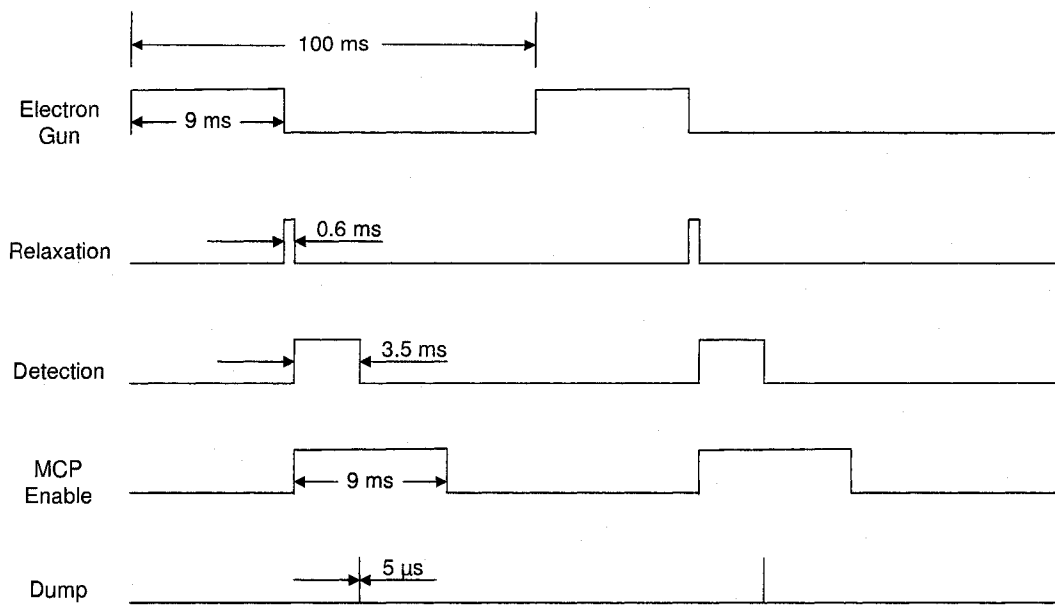


Figure 10 Experimental Timing and Control Signals

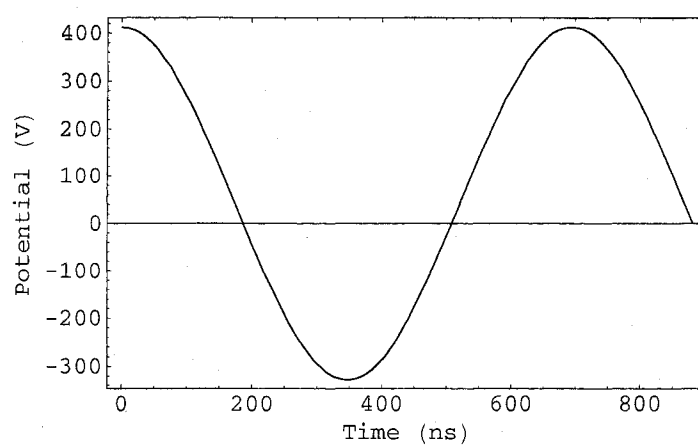
and elongated in the z direction. As this orientation of the ion cloud encounters the MCP, an output with broad peaks is produced.

When the rf potential is terminated as the rising edge of the sinusoidal waveform crosses the zero point [Fig.(12a)], however, the resulting ion time of flight signal that is observed on the oscilloscope has narrow peaks and sharp resolution. As Fig.(12b) illustrates, the rf field lines progress from the grounded endcap to the ring electrode. This is the opposite direction of the previous case. Therefore, as the positively charged ion cloud is ejected from the ion trap, it is elongated in the x direction and compressed in the z direction as it is attracted to the negatively charged ring electrode. As this orientation of the ion cloud encounters the MCP, an output with narrow peaks is produced. This approach was used in this experiment.

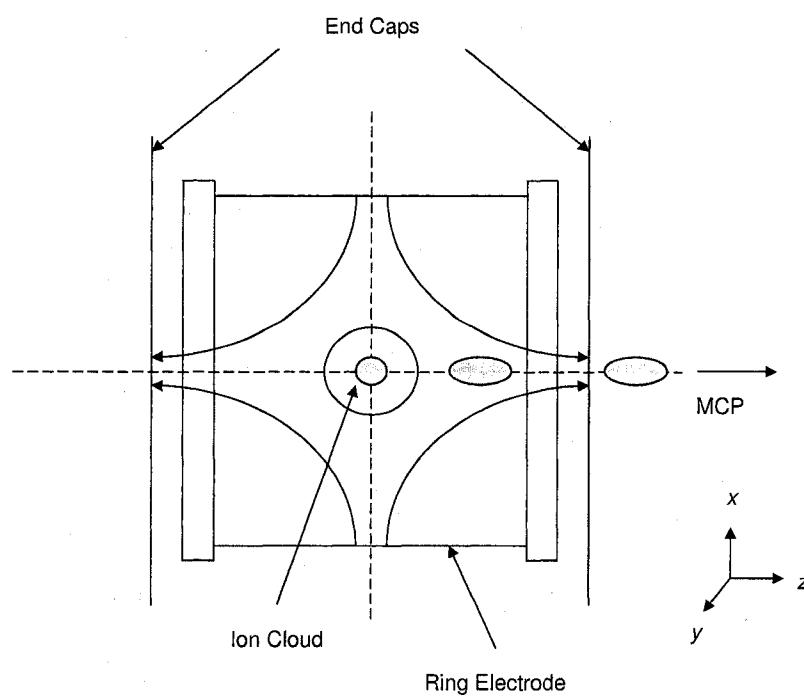
Data Acquisition/Analysis System

Figure 13 shows the data acquisition system used in this experiment. The output from the anode of the MCP is first sent to an amplifier that increases the signal output by a factor of 50. From there, the signal is sent to a Tektronix TDS 680C oscilloscope. The scope sweep is triggered by the rising edge of the ion dump pulse created by the IS-PIC. Since all the ions that are released from the trap see the same extraction potential, the time of flight of the ion is simply a function of its mass to charge ratio. The TOF spectrum is digitized by the oscilloscope and sent directly to a Gateway E-4200 computer for storage and data analysis.

Measurements of the ion signal intensity were made for a single dump delay at a specific N_2 pressure. These measurements were averaged with an automated data acquisition control software program and stored on the computers hard drive for future analysis. Measurements were then repeated for additional dump delays that spanned six different N_2 pressures. Origin was then used to analyze the data and extract the decay rates of N^{2+} and the charge transfer rate coefficient between N^{2+} and N_2 . A more in depth analysis of these processes will be presented in the following chapter.

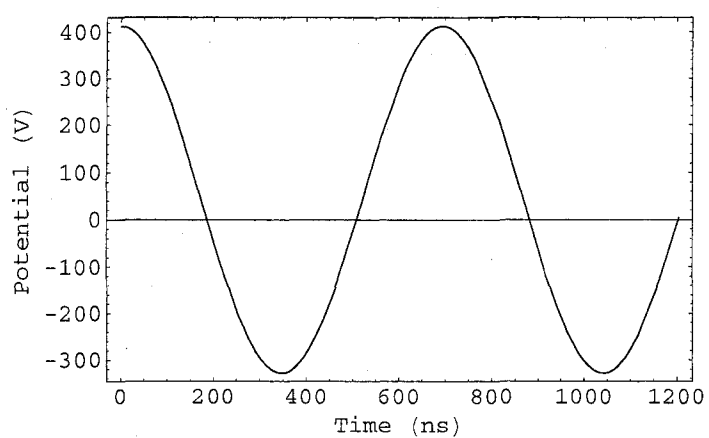


a)

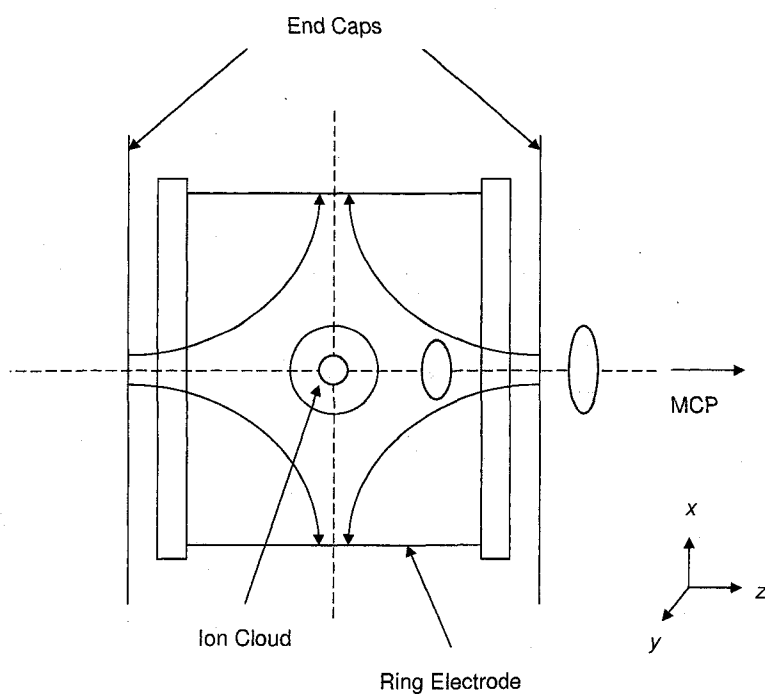


b)

Figure 11 a) RF Terminated on Falling Edge b) Field Lines Within Ion Trap



a)



b)

Figure 12 a) RF Terminated on Rising Edge b) Field Lines Within Ion Trap

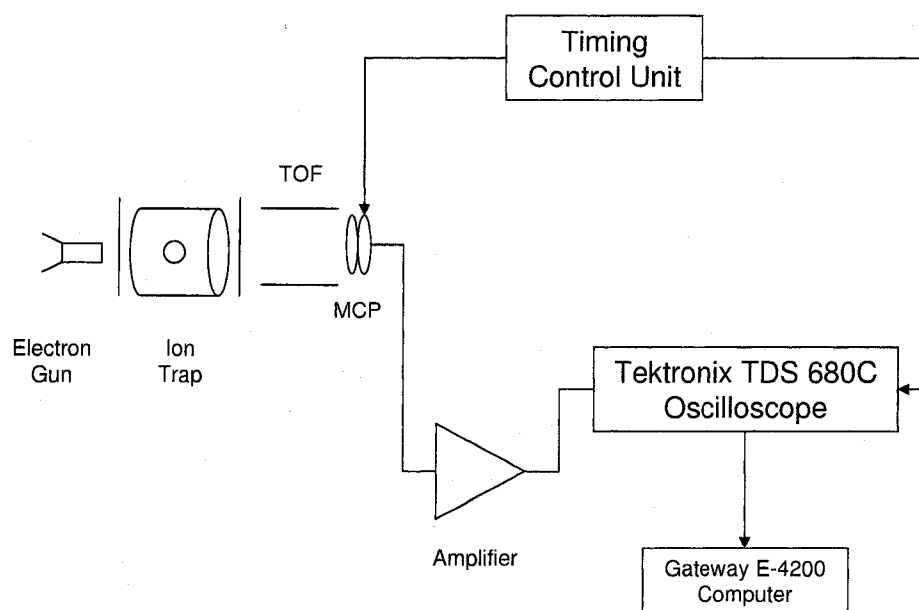


Figure 13 Data Acquisition and Analysis System

CHAPTER 4

EXPERIMENTAL METHODS AND PROCEDURES

Experimental Method and General Procedure

In this experiment, the charge transfer rate coefficient between N^{2+} and N_2 is determined by measuring the relative number of N^{2+} ions remaining in the ion trap as a function of time after production and particle density of the N_2 target gas. The number of N^{2+} ions present in the ion trap is determined by extracting them from the trap and detecting them with a multichannel plate (MCP). The time dependent profile of the ion signals amplitude is digitized by an oscilloscope and stored on a computer for subsequent data analysis.

The charge transfer rate coefficient is dependent on the energy states of the N^{2+} ions [1]. After N^{2+} ions are created by electron impact ionization, they can be found in both the ground and metastable states [53]. N^{2+} has a single low lying $2s2p^2(^4\text{P})$ metastable state with three fine structure levels ($^4P_{1/2}$, $^4P_{3/2}$, and $^4P_{5/2}$). All three levels decay by means of electric dipole spin-changing transitions to the $2s^22p(^2\text{P}^0)$ ground state. Their lifetimes are 0.98 ms, 13.4 ms, and 3.2 ms respectively [50]. Therefore, during the measurement time frame used in this experiment (29 ms to 189 ms after ion creation) any stored metastable N^{2+} ions should have decayed to the $2s^22p(^2\text{P}^0)$ ground state.

When the N^{2+} ions are in the ground state, the resulting decay curve can be described by a simple exponential function [9]:

$$I = I_0 e^{-Ct}, \quad (4.1)$$

where

$$C = n \langle Qv \rangle + \sum n' \langle Q'v' \rangle. \quad (4.2)$$

I_0 and I are the N^{2+} ion signal intensities at time zero and time t respectively. $\langle Qv \rangle$ and $\langle Q'v' \rangle$ are the charge transfer rate coefficients of N^{2+} with the N_2 target gas and N^{2+} with the residual background gases in the vacuum system. Q and Q' are the charge transfer cross sections of N^{2+} with the reactant N_2 gas and the residual background gas in the system respectively, while v and v' are the relative velocities of the interacting multiply charged ions with reactant gas molecules and residual gas molecules respectively. Finally, n is the particle density of the reactant N_2 gas and n' is the particle density of the residual background gas in the ultrahigh vacuum chamber.

Solving Eq.(4.1) for the decay constant (C), one gets

$$\ln(I) = -Ct + \ln(I_0). \quad (4.3)$$

Since the relationship is now linear, the decay constant (C) can be obtained by performing a least-squares fit to the time dependent N^{2+} ion signal intensity [Fig.(14)]. Six decay constants were obtained for six different N_2 target gas densities. According to Eq.(4.2), the charge transfer rate coefficient ($\langle Qv \rangle$) between N^{2+} and N_2 is obtained from the slope of the decay constants (C) versus the corresponding particle densities (n). The intercept gives the value of $\sum n' \langle Q'v' \rangle$, the charge transfer rate of N^{2+} with the residual background gases in the vacuum system. From this value, the charge transfer rate coefficient between N^{2+} and the main component of the residual background gas can be determined. The particle densities (n and n') can accurately be determined using the Masstorr DX100.

Several steps have to be carried out before the measurement of the charge transfer rate coefficient between N^{2+} and N_2 can be made. First, a detectable amount of N^{2+} ions needs to be created. Next, the N^{2+} ions need to be stored in the ion trap. Subsequently, the stored N^{2+} ions need to be detected. After the measurements are made, the final step is data analysis.

Creation of N^{2+}

The N^{2+} ions needed for this experiment are created by the electron impact ionization of ultrahigh purity (99.9999%) N_2 gas within the confines of the ion trap. As mentioned in

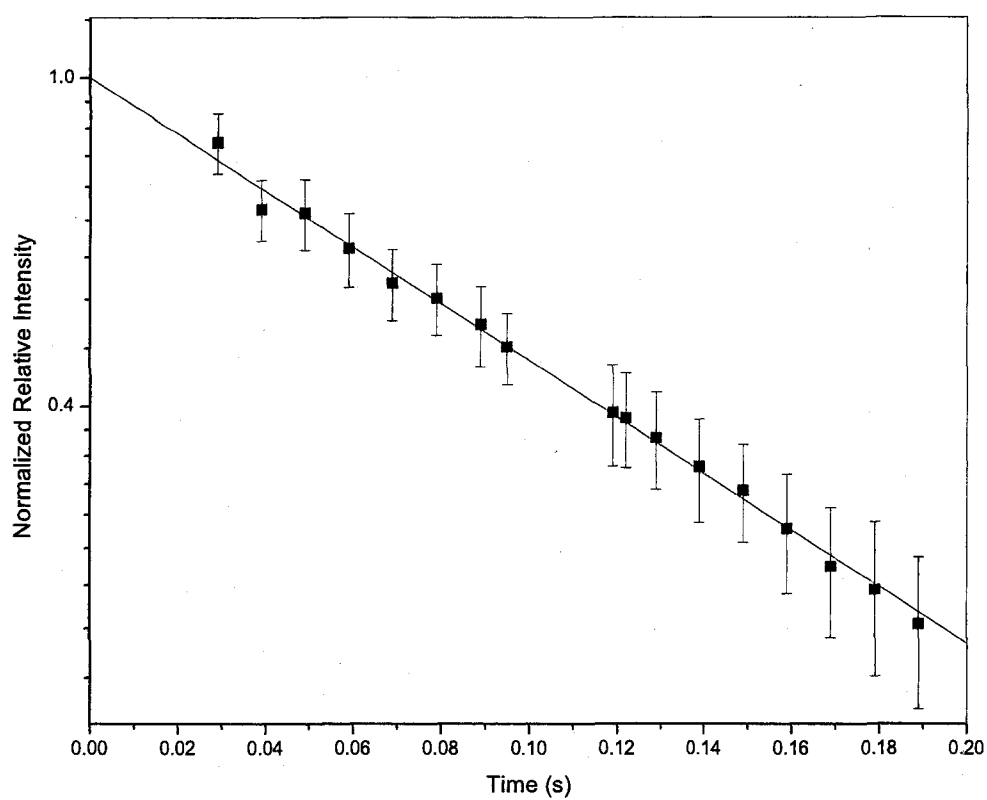


Figure 14 Least-Squares Fit of a Typical Time Dependent N_2^+ Signal

N_2 @ 1.04×10^{-7} Torr

Chapter 3, the electrons are supplied by an electron gun located just outside one of the end caps of the ion trap. The electron gun is outfitted with a negative and positive potential bias whose switching time from -150 V to $+123$ V is controlled by the IS-PIC generated TTL timing signal. The period of time that the electron gun is allowed to stream electrons into the trap (9 ms) is long enough to create a sufficient number of N^{2+} ions.

In order to ensure that the influence of contaminants on the measurement was negligible, a high vacuum of around 5×10^{-11} Torr was maintained in the vacuum chamber when the system was not in use. The composition of the residual background gas is shown in Fig.(15). It is mainly comprised of C, CH_3 , H_2O , and CO.

Ion Selection and Storage

Ions created by electron impact ionization can reside in a variety of charge states. In this experiment, electron bombardment of the N_2 target gas predominantly results in the creation of both N^+ ($\frac{m}{q} = 14$) and N^{2+} ($\frac{m}{q} = 7$). The rf quadrupole ion trap, however, can be used to select a particular ion charge state for study. Specific ion charge states can be stored in the ion trap by carefully choosing the trapping parameters (f , V_0 , U_0).

The locations of the N^+ and N^{2+} charge states on the ion trap stability diagram were investigated at various trapping parameters (f , V_0 , U_0). The results showed that:

1. $f = 1.44$ MHz, $V_0 = 350$ V, $U_0 = 29$ V;

N^{2+} lies within the stable region as shown in Fig.(16a). This will result in N^{2+} being stored within the ion trap. As a result of these trapping parameters, however, N^+ will also be confined within the ion trap [Fig.(16a)]. Since N^+ has a lower ionization energy (14.5 eV) than N^{2+} (44 eV), large quantities of N^+ can be created through electron bombardment and stored within the trap.

2. $f = 1.44$ MHz, $V_0 = 370$ V, $U_0 = 42$ V;

N^+ is out of the stability region and cannot be trapped. N^{2+} is located at the edge of the stable region, so it can be trapped [Fig.(17a)].

In order to test the physical system, the trapping parameters (f , V_0 , U_0) were set to the

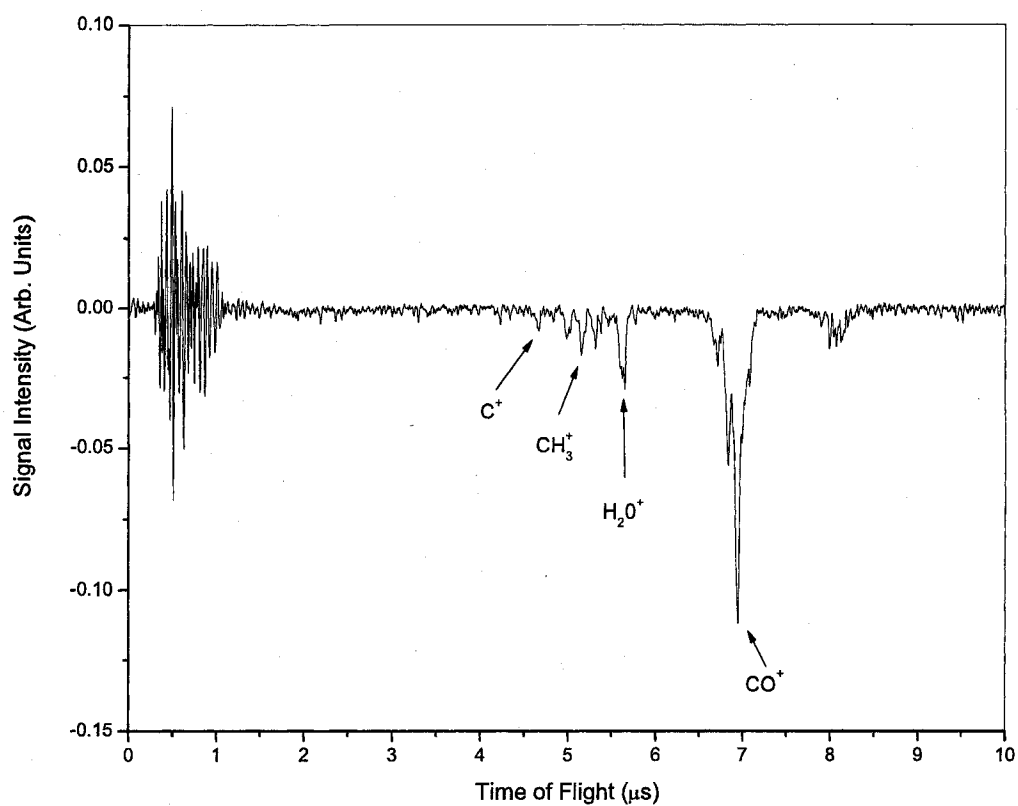
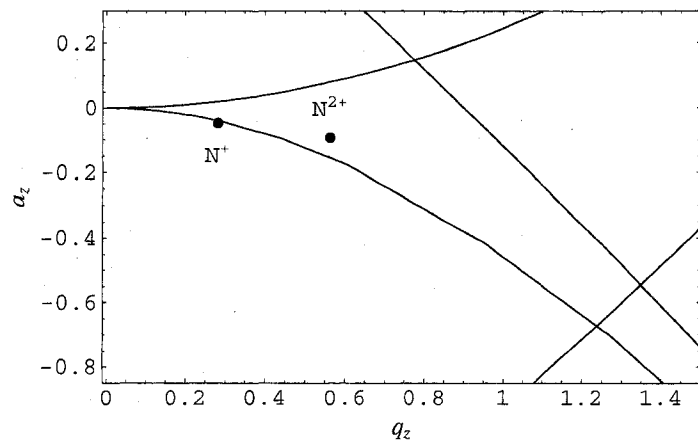
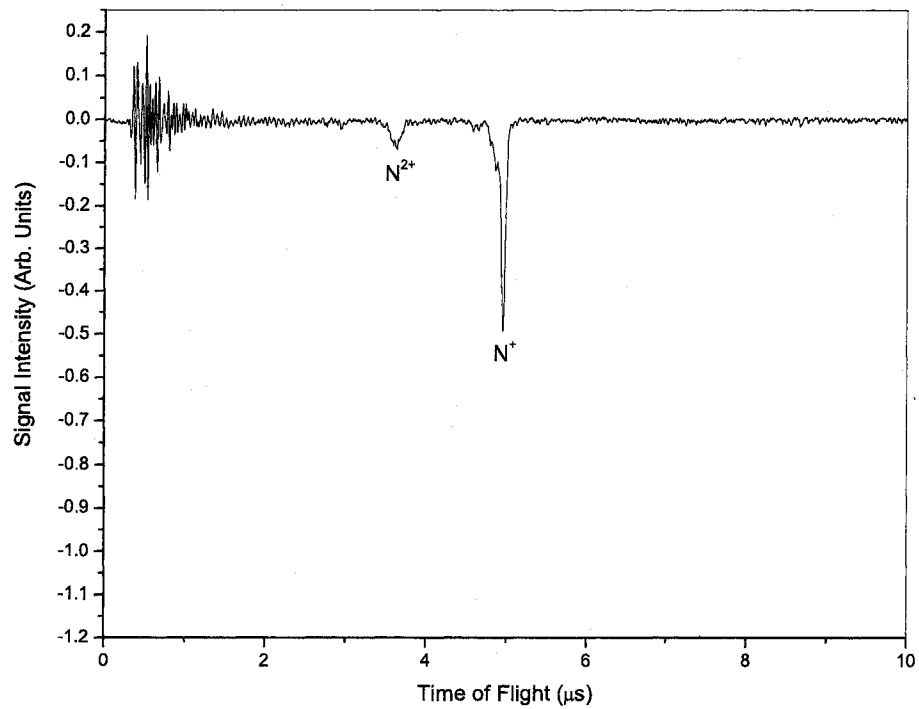


Figure 15 Residual Background Gas

$f = 970 \text{ kHz}$, $V_0 = 280 \text{ V}$, $U_0 = 14 \text{ V}$



a)

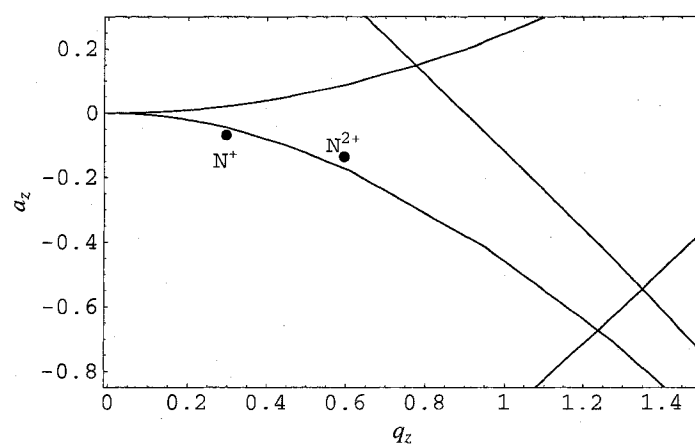


b)

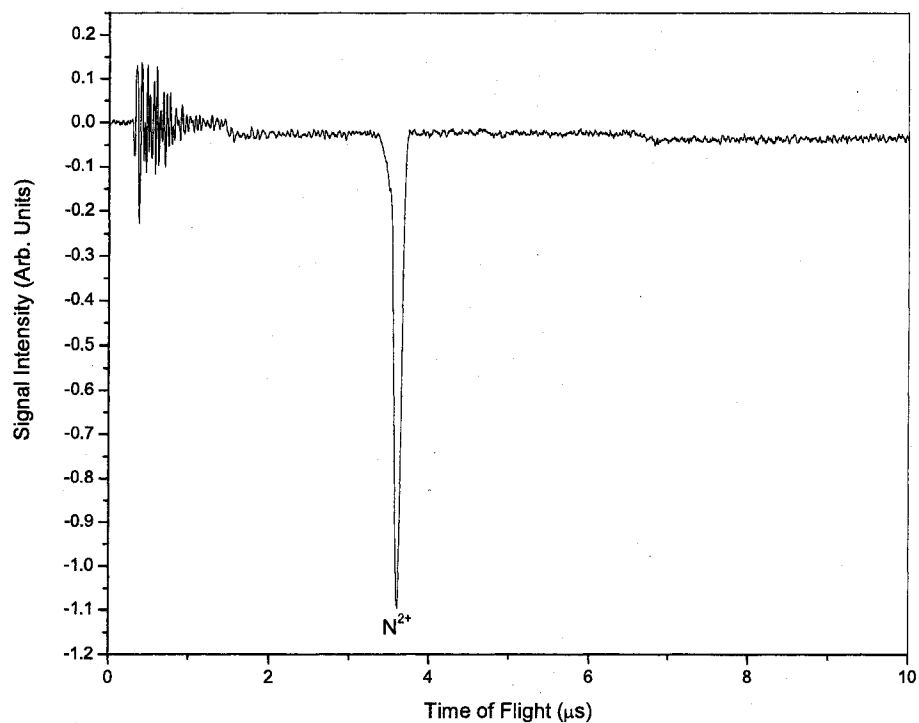
Figure 16 a) Stability Diagram for N^+ and N^{2+} b) Time of Flight for N^+ and N^{2+}

$$f = 1.44 \text{ MHz}, V_0 = 350 \text{ V}, U_0 = 29 \text{ V}$$

$$N_2 @ 5.80 \times 10^{-8} \text{ Torr}$$



a)



b)

Figure 17 a) Stability Diagram for N^+ and N^{2+} b) Time of Flight for N^{2+}

$$f = 1.44 \text{ MHz}, V_0 = 370 \text{ V}, U_0 = 42 \text{ V}$$

$$N_2 @ 5.80 \times 10^{-8} \text{ Torr}$$

values mentioned in 1 and 2. A push/pull voltage, which is gated on by the rising edge of the dump pulse, is applied to the trap's end caps. This will drive the N^{2+} ions out of the trap and toward the TOF tube and the MCP, which is gated on by the rising edge of the detection pulse. The ion signals obtained are shown in Fig.(16b) and Fig.(17b). N^{2+} can easily be identified using the time of flight technique [Eq.(3.17)]. When the trap parameters are set to confine both N^{2+} and N^+ , two ion peaks can be observed. But when the parameters are changed to store just N^{2+} , only one ion peak is present. Therefore, the experimental results and the stability diagram method are in agreement. When the N_2 gas supply is valved off, no signal is observed.

For the duration of the experiment the trapping parameters were set as follows: $f = 1.44$ MHz, $V_0 = 370$ V, $U_0 = 42$ V. These parameters were chosen because when combined, they resulted in only N^{2+} ions being stored within the ion trap. Therefore, any contamination from N^+ can be ruled out. In addition, these parameters generate a pseudopotential well for N^{2+} with an axial well depth of $D_z = 17.5$ eV and a radial well depth of $D_r = 46.4$ eV. Therefore, the probability of N^{2+} being kicked out of the trap due to elastic collisions with reactant N_2 gas at room temperature (0.04 eV) is very small. The pseudopotential also facilitates the storage of N^{2+} ions with a mean energy of 1.7 eV. This mean energy corresponds to an ion temperature of about 1.3×10^4 K [Eq.(3.14)]. According to Eq.(3.15), the equivalent temperature for each measurement is estimated to be 9.1×10^3 K.

Ion Detection

In order to detect the N^{2+} ions that are contained within the ion trap, the IS-PIC first has to create the ion ejection, or dump, pulse. The rising edge of this 1 ms pulse triggers the momentary shut off of the rf frequency (f), rf amplitude (V_0), and DC bias (U_0) being applied to the ring electrode of the ion trap in order to confine the N^{2+} ions. Simultaneously, the rising edge of the dump pulse triggers a 1 ms -225 V negative bias pulse that is applied to the end cap electrode of the trap facing the TOF tube and a $+236$ V positive bias pulse that is applied to the end cap electrode facing the electron gun. All this is done to ensure that the entire population of stored N^{2+} ions is extracted from the ion trap.

While the N^{2+} ions are being extracted from the trap, a -1400 V potential difference is applied to the time of flight tube. This accelerates the N^{2+} ions down the time of flight tube where they are eventually focused by an electrostatic lens potential of $+730$ V. After being focused, the N^{2+} ions encounter the multichannel plate (MCP). The MCP is gated on by the rising edge of the detection pulse and has a potential difference of $+1850$ V across it in order to accelerate the secondary electrons through its channels to the cathode. The output of the MCP is sent to and displayed on an oscilloscope which is also triggered by the rising edge of the dump pulse. Here the time of flight method [Eq.(3.17)] is once again used to identify that N^{2+} ions are indeed being stored within the ion trap [Fig.(17b)].

Pressure Calibration

For this experiment, a Masstorr DX100 ion gauge was used to determine the pressure of the N_2 target gas inside the vacuum chamber. Due to the different ionization potentials and cross sections of different gas molecules, the Masstorr DX100's filament has different ionization efficiencies for different gases. Thus, the pressure that is displayed on its digital readout is not an accurate representation of the pressure inside the vacuum chamber. Therefore, careful calibration of the Masstorr DX100 is required. Calibration is important because the particle density (n) of the N_2 target gas inside the vacuum chamber, in conjunction with the Boltzmann constant (k) and the temperature (T) of the N_2 target gas is used to determine the charge transfer rate coefficient between N^{2+} and N_2 . The particle density is directly proportional to the chamber pressure through the following correlation

$$n = \frac{P_{chamber}}{kT}. \quad (4.4)$$

The relationship between the pressure read from the Masstorr DX100 display and the actual pressure in the vacuum chamber is given by

$$P_{chamber} = \lambda P_{DX100}. \quad (4.5)$$

$P_{chamber}$ is the pressure inside the vacuum chamber, P_{DX100} is the pressure displayed by the

Masstorr DX100 (filament #2) in total mode, and λ is the conversion factor for a particular gas. A calibration of the filament used to measure the pressure of N_2 in this experiment was performed previously [53]. The absolute N_2 pressure in the vacuum chamber is $1.16 \pm 6\%$ times the pressure read from the Masstorr DX100 display ($\lambda = 1.16 \pm 6\%$).

Data Analysis

First, one hundred individual measurements of the N^{2+} signal intensity were taken at a specific dump delay (e.g. 29 ms) and N_2 target gas pressure (e.g. 3.60×10^{-8} Torr). The average and standard deviation of these one hundred measurements were calculated by an automated data acquisition program and stored in a computer's memory for future use [55]. This process of measuring, calculating, and storing was repeated for sixteen additional dump delays (39 ms, 49 ms, 59 ms, 69 ms, 79 ms, 89 ms, 95 ms, 119 ms, 122 ms, 129 ms, 139 ms, 149 ms, 159 ms, 169 ms, 179 ms, 189 ms) at the same N_2 target gas pressure (3.60×10^{-8} Torr). Next, five additional N_2 target gas pressures (5.80×10^{-8} Torr, 8.12×10^{-8} Torr, 1.04×10^{-7} Torr, 1.28×10^{-7} Torr, 2.44×10^{-7} Torr) were chosen. Measurements were then repeated for the same seventeen dump delays at each of the five additional N_2 target gas pressures. In the end, a total of 10,200 individual measurements were taken.

The automated data acquisition program uses the trapezoid rule to determine the area of the N^{2+} ion signal. The trapezoid rule works by approximating the region under the graph of a particular function by a trapezoid and calculating its area. In order to calculate the integral accurately, the interval of integration is first split into n smaller subintervals. The trapezoid rule is then applied to each of the smaller subintervals and those results are added together to determine the total N^{2+} ion signal area. In this experiment, the width of the N^{2+} ion signals were approximately 300 ns while each trapezoid was 4 ns wide.

Once the software program has calculated the area of each of the one hundred N^{2+} ion signal intensity measurements, it determines the average N^{2+} ion signal area and calculates the standard deviation (σ_y) with the following equation:

$$\sigma_y = \sqrt{\frac{1}{n-1} \sum_{i=1}^n (y_i - \bar{y})^2}. \quad (4.6)$$

Here n is the total number of measurements taken, y_i is the N^{2+} ion signal area from a given (x_i, y_i) ($i = 1, 2, \dots, n$) dataset, and \bar{y} is the average N^{2+} ion signal area. Each data point in Fig.(18) is the average of one hundred N^{2+} ion signal area measurements, and the standard deviation of those one hundred measurements is the uncertainty associated with that data point. Even though every point in Fig.(18) has an uncertainty associated with it, only a few are displayed to illustrate the general trend.

Next, Origin was used to perform linear fits to the data in Fig.(18) in order to obtain values for the N^{2+} decay constants (C). The uncertainties (σ_z) associated with the data points on the normalized semi-log (natural logarithm) plots [Fig.(20)-Fig.(25)] are a direct result of error propagation and are defined as

$$\sigma_z = \left| \frac{dz}{dy} \right| \sigma_y = \frac{\sigma_y}{y_i} \quad (4.7)$$

since z is of the form $\ln(I)$ [Eq.(4.1)]. Here y_i is the value of the N^{2+} ion signal intensity for a given data set (x_i, y_i) and σ_y is the standard deviation defined by Eq.(4.7) at that point.

Assuming a linear fit of the following form

$$y_i = A + Bx_i, \quad (4.8)$$

the slope (B) is calculated as follows

$$B = \frac{\sum_{i=1}^n w_i \sum_{i=1}^n w_i x_i y_i - \sum_{i=1}^n w_i x_i \sum_{i=1}^n w_i y_i}{\Delta}, \quad (4.9)$$

where

$$\Delta = \sum_{i=1}^n w_i \sum_{i=1}^n w_i x_i^2 - \left(\sum_{i=1}^n w_i x_i \right)^2 \quad (4.10)$$

and

$$w_i = \frac{1}{\sigma_z^2}. \quad (4.11)$$

The uncertainty (σ_B) in the slope (B) of the fit is determined by

$$\sigma_B = \sqrt{\frac{\sum_{i=1}^n w_i}{\Delta}}. \quad (4.12)$$

Once the decay rates (C) and statistical uncertainties (σ_B) were obtained, they were graphed against their respective particle densities (n) [Fig.(19)]. Another linear fit was then performed to determine the charge transfer rate coefficient ($\langle QV \rangle$) and associated uncertainty ($\sigma_{B'}$) [Eq.(4.2)]. In this case, the slope (B') of the fit and its estimated uncertainty ($\sigma_{B'}$) were calculated using Eq.(4.10), Eq.(4.11), and Eq.(4.12) with

$$w_i = \frac{1}{\sigma_B^2}. \quad (4.13)$$

CHAPTER 5

DISCUSSION OF RESULTS AND CONCLUSIONS

To determine the charge transfer rate coefficient between N^{2+} and N_2 , six sets of measurements were taken at different N_2 pressures ranging from 3.60×10^{-8} Torr to 2.44×10^{-7} Torr. All of the other parameters (f , V_0 , U_0) were fixed. Figure 18 is a plot of the N^{2+} ion signal intensity as a function of time for the six different N_2 pressures used in this experiment. The data points on each curve represent the mean of one hundred individual runs.

A typical normalized N^{2+} decay curve is shown in Fig.(14). A linear least-squares routine with a function of the form $y_i = A + Bx_i$ was used to fit the data and determine the decay constant (C). This was done for each of the six N_2 pressures [Fig.(20)-Fig.(25)]. The results of the fits are shown below in Table 1.

Table 1

N_2 Pressure (Torr)	Decay Constant (s^{-1})
3.60×10^{-8}	3.44 ± 1.16
5.80×10^{-8}	5.49 ± 0.98
8.12×10^{-8}	6.84 ± 0.66
1.04×10^{-7}	8.61 ± 0.76
1.28×10^{-7}	9.74 ± 0.70
2.44×10^{-7}	17.19 ± 0.76

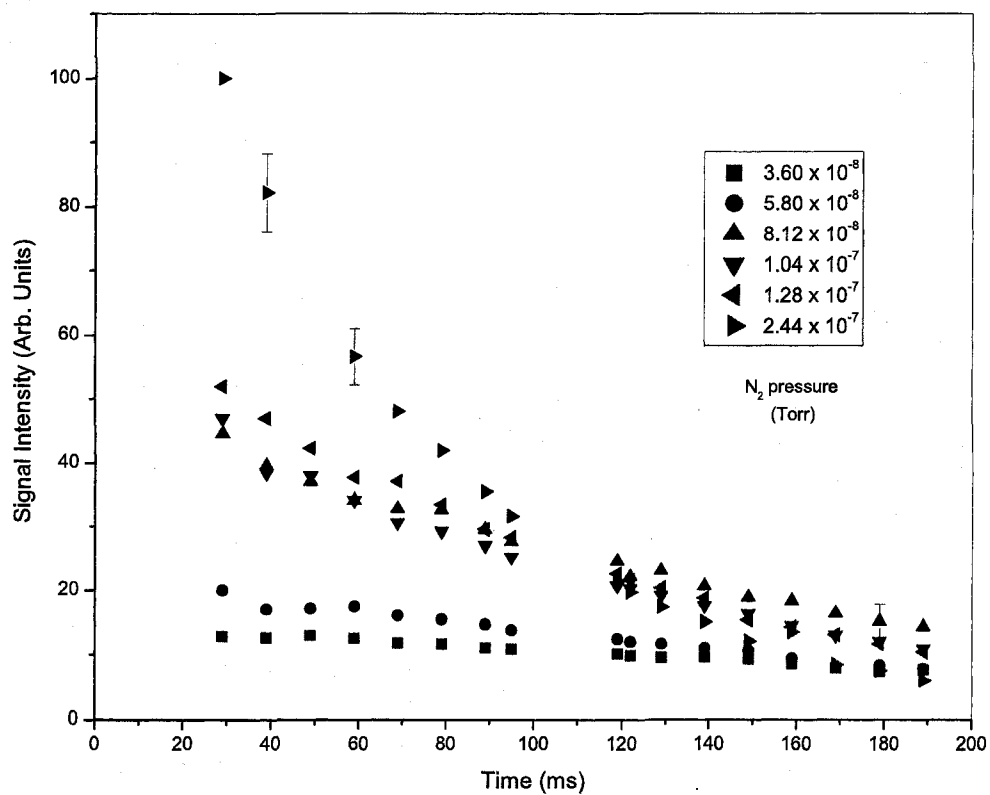


Figure 18 Decay Curves of N^{2+}

The decay constants were then plotted against their respective N_2 particle densities [Fig.(19)]. The slope of the straight line obtained from a least-squares fit to these six points is the charge transfer rate coefficient between N^{2+} and N_2 . In this experiment, the charge transfer rate coefficient between N^{2+} and N_2 is determined to be

$$\langle Qv \rangle = 1.95 \pm 0.27 \times 10^{-9} \text{ cm}^3 \text{ s}^{-1}. \quad (5.1)$$

This result is consistent with the previously measured result of $2.0 \pm 0.2 \times 10^{-9} \text{ cm}^3 \text{ s}^{-1}$ obtained by Fang and Kwong using laser ablation techniques and the same experimental facilities as this experiment [1]. It is also consistent with the value of $2.6 \pm 0.3 \times 10^{-9} \text{ cm}^3 \text{ s}^{-1}$ obtained by Wang and Church [56], and in agreement with the result of $2.8 \pm 0.6 \times 10^{-9} \text{ cm}^3 \text{ s}^{-1}$ acquired by Church and Holzschelter [57]. In both cases Church used a Penning trap and electron-impact ionization techniques.

The systematic and statistical sources of error in this experiment and the amount they contribute to the estimated uncertainty of the charge transfer rate coefficient are listed below in Table 2.

Table 2

Source of Error	% of Final Uncertainty in $\langle Qv \rangle$
Determination of Baseline	$\pm 1\%$
Calculation of Average N^{2+} Ion Signal Intensity	$\pm 10\%$
Decay Constant Fit (C)	$\pm 4\%$
Pressure Calibration	$\pm 6\%$
Charge Transfer Rate Coefficient Fit ($\langle Qv \rangle$)	$\pm 7\%$

Compared with the systematic error, the statistical error was dominant in this experiment. The estimated uncertainty of the charge transfer rate coefficient ($\pm 14\%$) is a quadratic sum of the uncertainty due to the systematic error associated with base line selections in

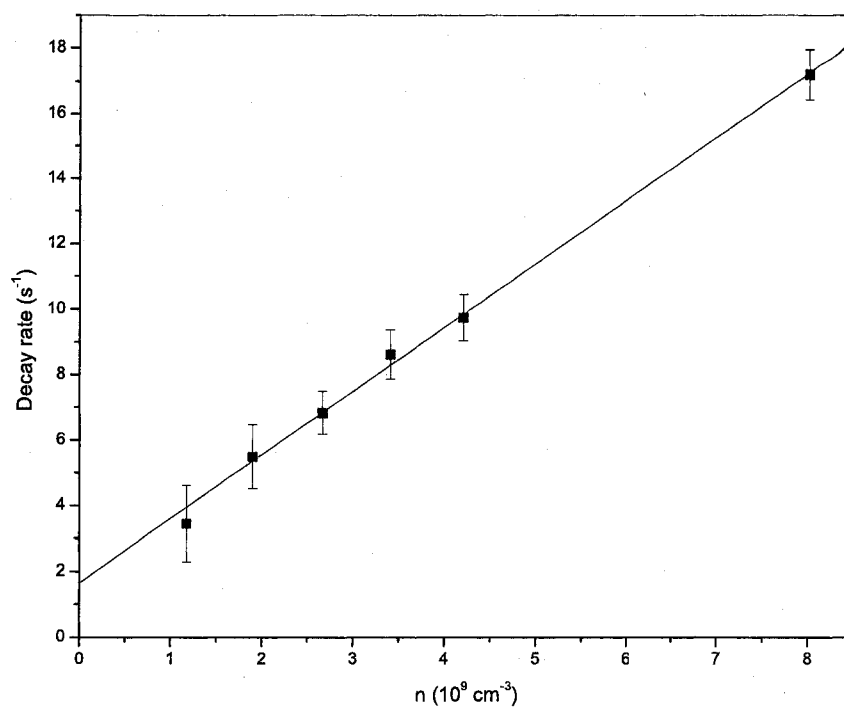


Figure 19 Charge Transfer Rate Coefficient Between N^{2+} and N_2

calculating the N^{2+} ion signal intensities and the statistical fluctuations present within the ion signal intensity, the data fitting, and the N_2 particle density measurements. It is calculated with the following equation

$$\delta\xi = \sqrt{(\delta a)^2 + (\delta b)^2 + (\delta c)^2 + (\delta d)^2 + (\delta e)^2}, \quad (5.2)$$

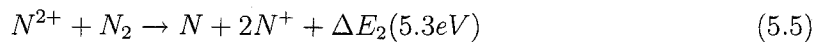
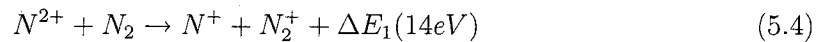
where $\delta\xi$ is the total uncertainty associated with the experimentally measured charge transfer rate coefficient and δa , δb , δc , δd , δe are the uncertainties listed in Table 2 respectively.

A number of conclusions can be drawn from this experiment. First off, it can be concluded that the ion gauge used in the experiment is calibrated since the experimentally determined value of the charge transfer rate coefficient is in agreement with the previously measured value that was obtained using the same experimental setup but a different ion source. Next, it can be concluded that Langevin theory gives a reasonable estimate on the charge transfer rate coefficient and cross section. The upper bound charge transfer rate coefficient from Langevin theory is given by

$$k_L = 2\pi q \left[\frac{\alpha}{\mu} \right]^{\frac{1}{2}} \quad (5.3)$$

where α is the polarizability of N_2 , q is the ionization state of N^{2+} , and μ is the reduced mass of the N^{2+} and N_2 system [56]. Using $\alpha(N^{2+}) = 1.7 \times 10^{-24} \text{ cm}^3$, a theoretical upper bound value of $k_L(N^{2+}, N_2) = 2.0 \times 10^{-9} \text{ cm}^3 \text{ s}^{-1}$ is obtained for the charge transfer rate coefficient. This value is consistent with the charge transfer rate coefficient of $1.95 \pm 0.27 \times 10^{-9} \text{ cm}^3 \text{ s}^{-1}$ obtained in this experiment.

The charge transfer reaction between N^{2+} and N_2 can be represented by the following two reactions:



Eq.(5.4) represents a single electron capture, while Eq.(5.5) represents a double electron capture. In the experiments performed in this thesis, the ion trap does not store the parent and product ions of the reactions listed in Eq.(5.4) and Eq.(5.5) at the same time due to the selection of the trapping parameters (f , V_0 , U_0) and the form of the pseudopotential they generate within the trap. In addition, since only the decay rate of the stored N^{2+} ions was measured in this experiment, there is no way to accurately determine the likelihood of single electron capture occurring instead of double electron capture even though double electron capture is much slower since it involves the transfer of two electrons at the same time.

Therefore, it is beneficial to examine the energy levels of the products listed in Eq.(5.4) and Eq.(5.5). Upon doing so, it becomes obvious that the product ions may not be located in their respective ground states since both reactions are exothermic and $\Delta E_1 > 0$, $\Delta E_2 > 0$. In Eq.(5.4), for example, a N^+ ion is formed when a N^{2+} ion captures an electron from N_2 . When this happens, the N^+ ion can be in either its $2s^2 2p^2(^3P_{2,1,0})$ ground state or one of its excited states. These excited states include: $2s^2 2p^2(^1D_2)$, $2s^2 2p^2(^1S_0)$, $2s 2p^3(^5S_2^0)$, $2s 2p^3(^3D_{3,2,1}^0)$, $2s 2p^3(^3P_{2,1,0}^0)$. The last two energy terms can decay to the ground state term by dipole transitions. Fortunately, each of these excited states is characterized by the wavelength of the photon emitted. The wavelength of the emitted photon can be identified with a narrow band interference filter. Therefore, a particular reaction process can be identified by looking for photons with specific wavelengths.

The merit of these excited states is questionable. Their presence inside tokamak fusion plasmas can ultimately be detrimental to the efficiency of the reactor itself. On the other hand, emission from these product ions or neutrals after they have undergone charge transfer provide invaluable information about the N_2 particle density and population ratios of a variety of ionization states of N^{q+} in astrophysical areas such as the interstellar medium.

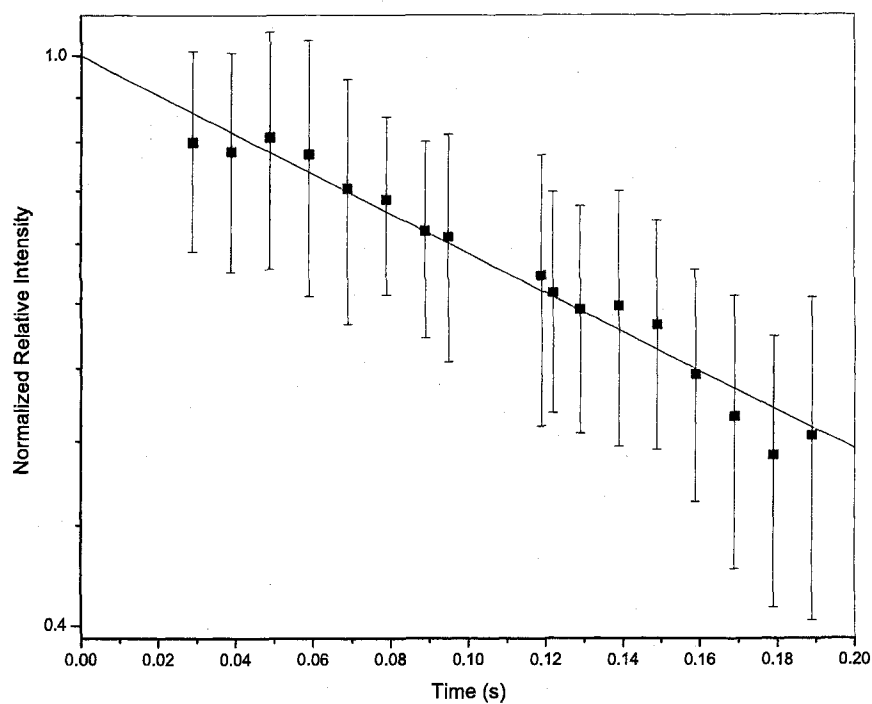


Figure 20 N_2^+ Decay Curve

N_2 @ 3.60×10^{-8} Torr

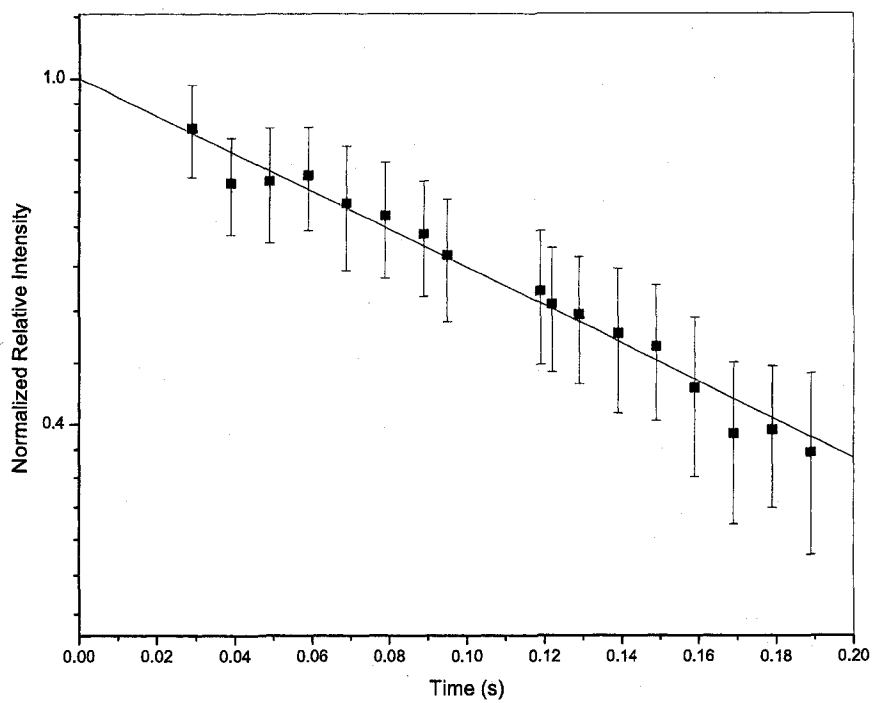


Figure 21 N_2^+ Decay Curve

N_2 @ 5.80×10^{-8} Torr

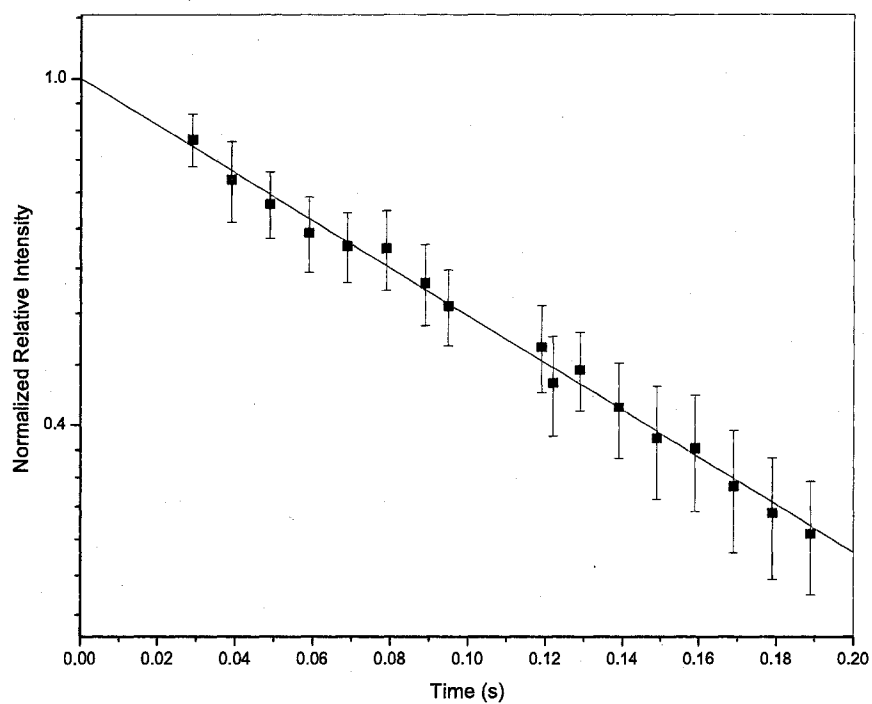


Figure 22 N_2^+ Decay Curve

N_2 @ 8.12×10^{-8} Torr

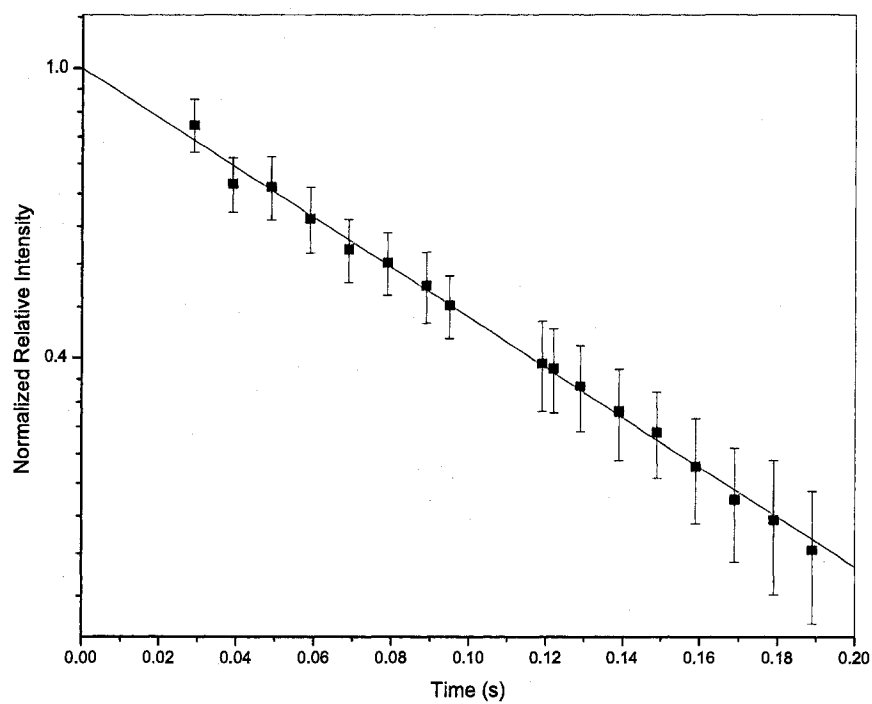


Figure 23 N_2^+ Decay Curve

N_2 @ 1.04×10^{-7} Torr

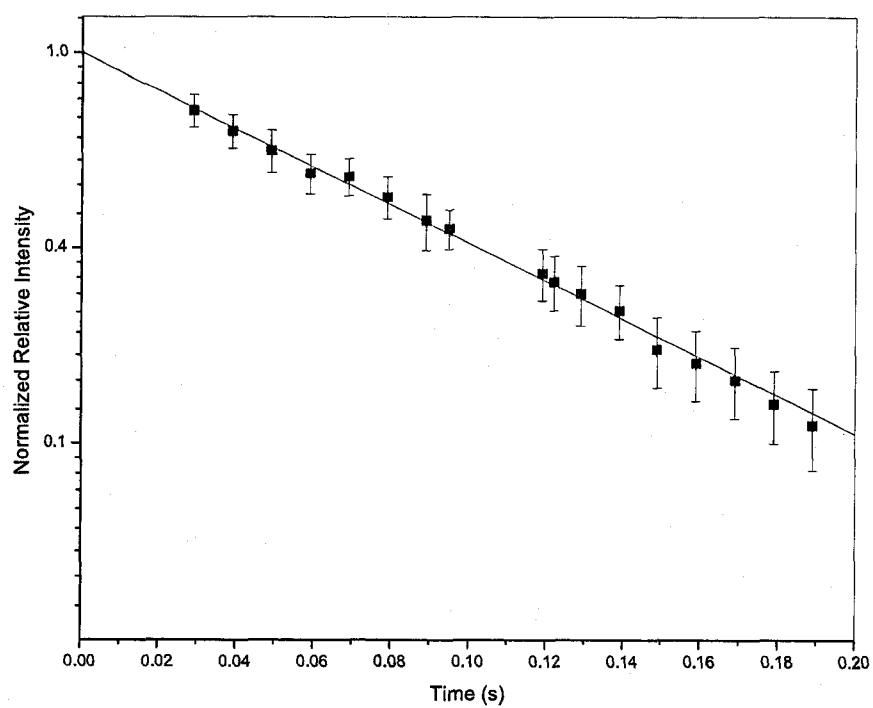


Figure 24 N^{2+} Decay Curve

N_2 @ 1.28×10^{-7} Torr

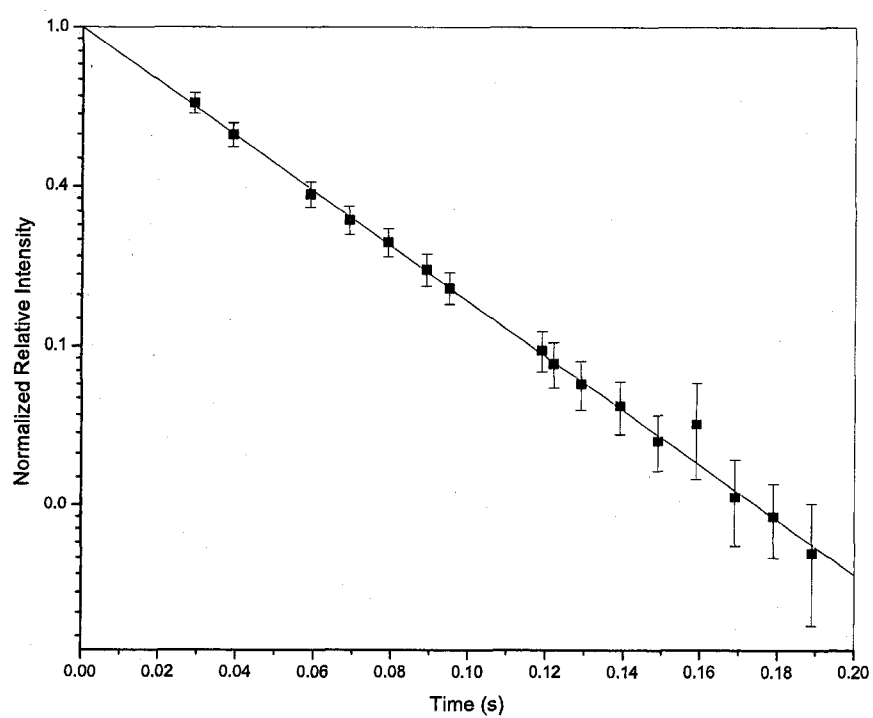


Figure 25 N_2^+ Decay Curve

N_2 @ 2.44×10^{-7} Torr

REFERENCES

- [1] Z. Fang and Victor H.S. Kwong, Phys. Rev. A 55, 440 (1997).
- [2] Hui Gao and Victor H.S. Kwong, Phys. Rev. A 69, 052715 (2004).
- [3] J. Wang, Ph.D. thesis, University of Nevada, Las Vegas (1997).
- [4] G.M. McCracken et al., J. Nuc. Mat. 37 266 (1999).
- [5] C.F. Melius, J. Phys. B 7, 1962 (1974).
- [6] Z. Fang and Victor H.S. Kwong, Phys. Rev. A 51, 1321 (1995).
- [7] M. Gargaud, M.C. Bacchus-Montabonel, and R. McCarroll, J. Chem. Phys. 99, 4495 (1993).
- [8] A. Dalgarno, S.E. Butler, and T.G. Heil, J. Geophys. Res. 85, 6047 (1980).
- [9] V.H.S. Kwong, T.T. Gibbons, Z. Fang, J. Jiang, H. Knocke, Y. Jiang, B. Ruger, S. Huang, E. Braganza, and W. Clark, Rev. Sci. Instrum. 61 1931 (1990).
- [10] D.A. Church and H.M. Holzschneider, Phys. Rev. Lett. 49, 643 (1982).
- [11] H.F. Winters and Inokuti, Phys. Rev. A 25, 1420 (1982).
- [12] Y. Sun, H.R. Sadeghpour, K. Kirby, and A. Dalgarno, Int. Rev. Phys. Chem. 15, 53 (1996).
- [13] A. Dalgarno, Nucl. Instrum. Methods B 9, 655 (1985).
- [14] G. H. Henderson, Proc. Roy. Soc. A 102, 496 (1923).
- [15] B.H. Bransden and M.R.C. McDowell, *Charge Exchange and the Theory of Ion-Atom Collisions* (Oxford University Press, New York, 1992).
- [16] L. H. Thomas, Proc. Roy. Soc. A 114, 561 (1927).
- [17] J.R. Oppenheimer, Phys. Rev. 31, 349 (1928).
- [18] H. C. Brinkman and H. A. Kramers, Proc. Acad. Scien. Amsterdam 33, 973 (1930).
- [19] I. Shimamura and K. Takayanagi, *Electron-Molecule Collisions* (Plenum Press, New York, 1984).
- [20] H. W. Massy and R. A. Smith, Proc. Roy. Soc. A 142, 142 (1933).
- [21] R. A. Baragiola and E. R. Salvatelli, Phys. Rev. A 12, 806 (1975).
- [22] K. Okuno, NISF Research Report ISSN 0915-6364 Apr. 2007.

- [23] H.G. Dehmelt, Adv. At. Mol. Phys., 3, 53 (1967).
- [24] R.D. Knight, Ph.D. thesis, University of California, Berkeley (1979).
- [25] W. Paul and H. Steinwedel, German Patent No. 944, 900, June 28, 1956.
- [26] K. Berkling, "Diplomarbeit", Physik. Inst. Univ. Bonn, German (1956).
- [27] E. Fischer, Z. Physik. 156, 26 (1959).
- [28] P.H. Dawson and N.R. Whetton, Dyn. Mass. Spec., 2, 1, (1971).
- [29] P.H. Dawson, Int. J. Mass Spec. Ion Phys., 14, 317 (1974).
- [30] P.H. Dawson, and M. Meunier, Int. J. Mass Spec. Ion Phys., 29, 269 (1979).
- [31] P.H. Dawson and C. Lambert, J. Vac. Sci. Tech., 12, 941 (1968).
- [32] P.H. Dawson and N.R. Whetton, J. Vac. Sci. Tech., 5, 1 (1968).
- [33] P.H. Dawson (ed.), "Quadrupole Mass Spectrometer and its Applications", Elsevier Scientific Pub. Co., New York (1976).
- [34] P.H. Dawson and C. Lambert, Int. J. Mass Spec. Ion Phys., 16, 269 (1975).
- [35] P.H. Dawson and C. Lambert, Int. J. Mass Spec. Ion Phys., 14, 339 (1974).
- [36] J.F.J. Todd and R.M. Waldren, Int. J. Mass Spec. Ion Phys., 29, 301 (1979).
- [37] J.E. Fulford and R.E. March, Int. Mass Spec. Ion Phys., 30, 39 (1979).
- [38] P.H. Dawson and N.R. Whetton, J. Vac. Sci. Tech., 5, 11 (1968).
- [39] P.H. Dawson, J. W. Hedman, and N.R. Whetton, J.Sci. Ins., 40, 1444 (1969).
- [40] P.H. Dawson and N.R. Whetton, Adv. Electron Phys., 27, 59 (1969).
- [41] G. Lawson and J.F.J. Todd, Chem. In Brit., 8, 373 (1972).
- [42] J.F.J. Todd, R.M. Waldren, R.E. Mather and G. Lawson, Int. J. Mass Spec. Ion Phys., 28, 141 (1978).
- [43] R.E. Mather, G. Lawson, and J.F.J. Todd, Int. J. Mass Spec. Ion Phys., 28, 347 (1978).
- [44] R.M. Waldren and J.F.J. Todd, Int. J. Mass Spec. Ion Phys., 29, 315 (1979).
- [45] G. Lawson, R.F. Bonner, and J.F.J. Todd, J. Phys. E: Sci Ins., 6, 357 (1973).
- [46] M. Benalin and Clande, Int. J. Mass. Spec. Ion Phys., 11, 421 (1973).
- [47] R.D. Knight, Int. J. Mass Spec. Ion Phys., 51, 127 (1983).
- [48] V.H.S. Kwong and Z. Fang, Phys. Rev. Lett. 71, 4127 (1993).
- [49] R.D. Knight and M.H. Prior, J. Appl. Phys., 50, 3044 (1978).
- [50] Z. Fang and Victor H.S. Kwong, Astrophysical J. 413, L141 (1993).

- [51] Brad Clarke, Private Discussions, 2007.
- [52] J. Jiang, Masters thesis, University of Nevada, Las Vegas (1989).
- [53] Y. Jiang, Masters thesis, University of Nevada, Las Vegas (1990).
- [54] Chrysanthos Kyriakides, Private Discussions, 2006.
- [55] Bill O'Donnell, Private Discussions, 2007.
- [56] Hua-Ying Wang and D. A. Church, Phys. Rev. A 36, 9 (1987).
- [57] D. A. Church and H. M. Holzschneider, Chem. Phys. Lett. 76, 109 (1980).

VITA

Graduate College
University of Nevada, Las Vegas

Wayn K. Ward

Local Address:

2801 Swallow Point Circle
Las Vegas, Nevada 89117

Bachelors of Science, Physics, 2004

Mesa State College
Grand Junction, Colorado

Publications:

Kwong, V. H. S., Kyriakides, C., and Ward, W. K. *Metastable State Populations in Laser Induced Plasmas*. Nasa Laboratory Astrophysics Workshop 2006, UNLV, Nevada, 2006.

Thesis Title: Charge Transfer Between N^{2+} and N_2 at Low Energies

Thesis Committee:

Committee Chairperson: Dr. Victor H. S. Kwong, Ph.D.

Committee Member: Dr. James Selser, Ph.D.

Committee Member: Dr. David Shelton, Ph.D.

Committee Member: Dr. Stephen Lepp, Ph.D.

Graduate Faculty Representative: Dr. Balakrishnan Naduvalath, Ph.D.